Separation length in high-enthalpy shock/boundary-layer interaction

Jean-Paul Davis[a] and Bradford Sturtevant
Graduate Aeronautical Laboratories, California Institute of Technology, Pasadena, California 91125

(Received 23 November 1999; accepted 29 June 2000)

Experiments were performed in the T5 Hypervelocity Shock Tunnel to investigate nonequilibrium real-gas effects on separation length using a double-wedge geometry and nitrogen test gas. Local external flow conditions were estimated by computing the inviscid nonequilibrium flow field. A new scaling parameter was developed to approximately account for wall temperature effects on separation length for a laminar nonreacting boundary layer and arbitrary viscosity law. A classification was introduced to divide mechanisms for real-gas effects into those acting internal and external to viscous regions of the flow. Internal mechanisms were further subdivided into those arising upstream and downstream of separation. Analysis based on the ideal dissociating gas model and a scaling law for separation length of a nonreacting boundary layer showed that external mechanisms due to dissociation may decrease separation length at low incidence but depend on the free-stream dissociation at high incidence. A limited numerical study of reacting boundary layers showed that internal mechanisms due to recombination occurring in the boundary layer upstream of separation cause a slight decrease in separation length relative to a nonreacting boundary layer with the same external conditions. Correlations were obtained of experimentally measured separation length using local external flow parameters computed for reacting flow, which scales out external mechanisms but not internal mechanisms. These showed the importance of the new scaling parameter in high-enthalpy flows, a linear relationship between separation length and reattachment pressure ratio, and a Reynolds-number effect for transitional interactions. A significant increase in scaled separation length was observed in the experimental data at high enthalpy. The increase was attributed to an internal mechanism arising from recombination in the free-shear layer downstream of separation, perhaps altering its velocity profile. This real-gas effect depends on the combined presence of free-stream dissociation and a cold wall.
[S1070-6631(00)51310-5]

I. INTRODUCTION

Interaction between a shock wave and a boundary layer can produce a region of separated flow. The phenomenon may occur, for example, at the upstream-facing corner formed by a deflected control surface on a hypersonic reentry vehicle, where the length of separation has implications for control effectiveness. Separation can also occur where a shock wave generated internally to a hypersonic air-breathing propulsion system impinges on a boundary layer. Thus separation length may be important in determining engine performance. In addition, knowledge regarding separation length in shock/boundary-layer interactions has relevance to separation length in supersonic wake flow.

The mechanisms by which nonequilibrium real-gas effects act to change separation length in high-enthalpy shock/boundary-layer interaction are poorly understood. Previous experiments have either explored regimes where real-gas effects are insignificant or have not found conclusive results, and while several computational studies have found different real-gas effects under different conditions, nowhere in the existing literature is there presented a unified explanation of the mechanisms involved (see Sec. I A 2). The objective of the present work is to develop a framework for describing mechanisms for real-gas effects in shock/boundary-layer interaction, and where possible, to validate these mechanisms by experiments (in the T5 Hypervelocity Shock Tunnel at Caltech) and by comparison to previous results in the literature.

The present study is limited to two-dimensional interactions generated by an upstream-facing corner on a double wedge, an abstraction of flow on a reentry vehicle at angle of attack with deflection of a trailing body flap. To remove as many complications as possible, we consider only a sharp leading edge and work with nitrogen, a binary dissociating gas. The experiments in T5 include transitional and turbulent interactions, but the emphasis in this work is on purely laminar interactions. While hypervelocity shock tunnels have the important advantage of being able to simulate the high enthalpies of reentry conditions, it should be noted that the experimental test conditions cannot precisely duplicate flight conditions on a scaled model, for the following three reasons: (1) the free stream in a shock tunnel is partially dissociated at high enthalpy; (2) dissociation and recombination reaction rates depend differently on density, and only one of them can be properly scaled even if both are present; (3) the ratio of wall to free-stream temperature is smaller for high-

[a]Present address: Sandia National Laboratories, Albuquerque, New Mexico 87185; electronic mail: jpdavis@sandia.gov

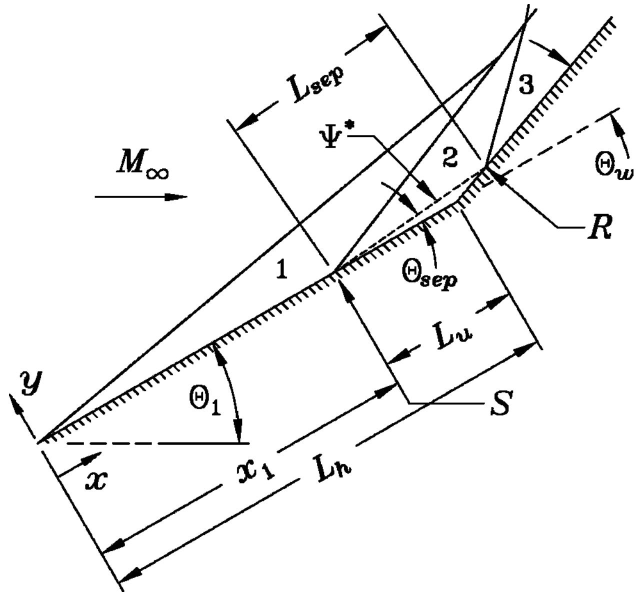

FIG. 1. Schematic of separated flow on a double wedge with definitions for the notation used throughout this work.

enthalpy shock tunnel experiments than for hypervelocity flight. The present approach is to use the capabilities of the T5 Hypervelocity Shock Tunnel to explore the physics of the problem, regardless of relevance to a particular reentry flight trajectory.

Figure 1 presents a schematic of the separated double-wedge flow field and defines notation used throughout this article. The boundary layer separates upstream of the corner (or hingeline) at S and reattaches downstream at R. Between S and R, the dividing streamline ψ^* (approximated by a straight line) is defined as the streamline through which there is no mass flux. The inviscid flow regions ∞ and 1–3 are generally not uniform as implied by Fig. 1. The following restricted definitions apply when discussing the present experiments: ∞ refers to free-stream conditions on the nozzle centerline at the leading edge of the double wedge; 1 refers to the edge of the boundary layer just upstream of S; 2 and 3 refer to consistently defined locations based on experimental and computational data.

The ambiguous phrase ''real-gas effects'' is here defined as changes in a flow field due to chemical and thermal nonequilibrium, with respect to the same flow without chemical reactions and without vibrational relaxation. It is imperative to note exactly what is the nonreacting reference flow; confusion can arise particularly in connection with shock-tunnel flows for which the nonreacting reference flow includes partial dissociation.

A. Review of previous work

1. Perfect-gas flows

The phenomenon of shock/boundary-layer interaction has been studied extensively for perfect-gas flows during the past four decades, using experimental and analytical–computational techniques. The length of separation depends on parameters which characterize the incoming boundary layer, the free-shear layer, and the reattachment pressure rise. These include the local Reynolds number Re_{x_1} and Mach number M_1 at separation, the wall-to-edge temperature ratio T_w/T_1, the flap deflection θ_w, and the ratio of specific heats γ_1. Separation length must also be proportional to a length scale; if the downstream edge of the ramp does not influence the reattachment region, the only length scales are the distance from the leading edge x_1 and the boundary-layer thickness δ_1, itself a function of x_1 as well as Re_{x_1}, M_1, T_w/T_1, and γ_1.

Clearly, L_{sep} should increase with increasing flap deflection θ_w, or equivalently, with increasing reattachment pressure ratio p_3/p_2. This has been confirmed numerous times both by experiments[1–15] and by computations,[2,16–20] regardless of whether the interaction is laminar, transitional, or turbulent. L_{sep} has also been shown without exception, both experimentally and computationally, to increase with decreasing M_1.[4,6,8,11,12,18,21–24] For purely laminar interactions, L_{sep} increases with increasing Re_{x_1}.[11,19,21,22,25–27] Experiments with transitional interactions all show L_{sep} decreasing with increasing Re_{x_1}, due to upstream movement of transition in the shear layer.[5,6,25,27,28] Results for purely turbulent interactions depend on the range of Re_{x_1} investigated; some experiments show L_{sep} increasing with Re_{x_1} (Refs. 3, 4, 23, and 28) while others show the opposite.[13,15,24] Hunter and Reeves[29] found by computation that L_{sep} increases with Re_{x_1} for transition upstream of separation but downstream of the leading edge, with the trend reversing when transition reaches the leading edge. Both turbulent regimes produce much smaller separation bubbles than the laminar regime.

For purely laminar or turbulent interactions, L_{sep} has been shown to increase with increasing T_w/T_1,[4,5,12,19,23,26,30–33] the effect being much stronger for laminar interactions. There are conflicting results for transitional flows; experiments by Johnson[25] showed L_{sep} increasing with T_w/T_1, while experiments by Coët and Chanetz[31] show the opposite trend. The latter was attributed to the effect of T_w/T_1 on shear-layer stability and location of transition. The importance of the incoming boundary-layer profile in determining L_{sep} was shown clearly by Hayakawa and Squire,[8] who found that injecting gas through a porous wall upstream of a turbulent interaction had the effect of reducing skin friction and increasing separation length.

2. Real-gas effects

The presence of real-gas effects introduces the additional parameters of stagnation enthalpy (h_0) and reaction rate, the latter difficult to characterize in a global sense for high-enthalpy, viscous separated flow. The review in this section encompasses, to the authors' knowledge, all results published before 1998 pertaining to real-gas effects on separation length in two-dimensional interactions.

Two experimental studies of compression-corner flows have been carried out in the T3 Shock Tunnel at the Australian National University. Rayner[34] considered a double wedge with $\theta_1 = 18.5°$, $\theta_w = 30°$, and variable L_h. Separation length was found to initially decrease with increasing h_0 and then increase again at high enthalpy, but was not correlated independently of other parameters. The decrease with h_0 may be consistent with perfect-gas results since Re_∞ and T_w/T_1 both decrease for shock tunnel flows as h_0 is increased, but M_∞ decreases at the same time. The conditions in T3 with $h_0 > 25$ MJ/kg have subsequently been shown to suffer from significant helium driver-gas contamination.[35] Mallinson *et al.*[36,37] considered a flat plate with $\theta_1 = 0°$ and $5° \leqslant \theta_w \leqslant 24°$. They concluded that real-gas effects on the interaction were negligible under the conditions investigated, because dissociation rates downstream of oblique shocks in shock tunnel flows remain insignificant for moderate shock angles,[38] and dissociation in the boundary layer was found to be negligible even at the highest-enthalpy conditions.[39] The free stream at high enthalpy was partially dissociated, but effects due to recombination were not considered.

Other experimental studies[40,41] looked at axisymmetric configurations abstracted from the windward centerline of either the Hermes reentry vehicle (hyperboloid-flare geometry) or the Shuttle Orbiter (HAC geometry), corresponding to flight at 30°–35° angle of attack with a trailing body flap deflected 20°. Krek *et al.*[40] found an apparent reduction in L_{sep} with increasing h_0 at constant $\overline{V}_\infty = M_\infty/\sqrt{\mathrm{Re}_\infty}$ for the hyperboloid-flare geometry in the HEG shock tunnel at the DLR in Germany. Experiments by one of the authors (J.-P. D.)[41] on the HAC geometry in the T5 shock tunnel, however, showed no such trend with enthalpy when correlated in the same manner.

Anders and Edwards[21] applied an analytical procedure to compression-corner flows with $M_1 \simeq 12$ and $h_0 \lesssim 12$ MJ/kg, and found that chemical equilibrium resulted in smaller L_{sep} compared to chemically frozen flow at the same conditions. For most of the equilibrium results, L_{sep} increased with increasing h_0; this trend reversed at $h_0 \lesssim 5$ MJ/kg for large separation regions at high θ_w.

The result that separation length decreases for reacting flows relative to frozen flows was found in a number of computational studies on compression-corner flows,[17] axisymmetric hyperboloid-flare flows,[42–44] and shock-impingement flows.[45] When there is negligible dissociation upstream of reattachment (see Furumoto *et al.*[45] or Grasso and Leone[17]), the decrease in L_{sep} may be due to lower pressure in region 3 caused by dissociation behind the reattachment shock. An explanation is not so obvious for the results of Oswald *et al.*,[43] Brenner *et al.*,[42] or Kordulla *et al.*,[44] all of whom compared frozen flow to equilibrium flow on the hyperboloid flare. To complicate matters, the comparison by Oswald *et al.*[43] was between an equilibrium flight condition at $M_\infty = 25$ and a perfect-gas wind tunnel condition at $M_\infty = 10$. In these studies, dissociation occurs in region 1 due to the bow shock, which increases M_1 but also results in higher p_3 than for frozen flow.

Ikawa[46] also found a reduction in L_{sep} for reacting flow, using a momentum integral technique extended to include the species conservation equation for a binary dissociating gas, and taking either fully dissociated or fully recombined boundary-layer edge conditions with a fully recombined wall condition. The approach assumes that binary diffusion dominates production of molecules by recombination. The case with dissociation at the boundary-layer edge showed a thinner boundary layer (which Ikawa attributes to the diffusion circuit set up in the boundary layer) and a smaller separation bubble.

Real-gas effects on separated shock-impingement flows were studied computationally by Ballaro and Anderson[47] and by Grumet *et al.*[48] for dissociated upstream conditions corresponding to flow that has expanded around a blunt body after being processed by a Mach 25 normal shock. For separation length in nonequilibrium flow compared to frozen flow, Ballaro and Anderson[47] found a slight decrease at the two Reynolds numbers investigated, while Grumet *et al.*[48] found a slight decrease at low pressure and a large increase at high pressure. In the latter case, the large increase in L_{sep} was attributed to strong recombination in the recirculation region at high pressure. Reasons for the decrease in L_{sep} under other conditions are not obvious; only Ballaro and Anderson give pressure results, showing increased p_3 for nonequilibrium flow. Both of these studies have separation occurring close to the leading edge of the computational grid, which raises the question of whether or not the separation point is unintentionally fixed. Grumet *et al.*[48] also considered the effect of wall catalyticity, and found that L_{sep} was larger for a fully noncatalytic than for a fully catalytic wall, the difference being less pronounced at the high-pressure condition where gas-phase recombination dominates.

B. Overview of present work

Experimental measurements from double-wedge flows in the T5 shock tunnel provided insight into real-gas effects on separation length, but only after extensive analysis to reconstruct properties of the flow field and to understand expected real-gas behavior from a theoretical viewpoint. Thus, while the experimental methods are described first in Sec. II, the experimental results for separation length are not presented until much later in Sec. VI. The advanced computational technique used to estimate local flow parameters for each experiment and to study viscous aspects of the flow is presented in Sec. III along with comparisons to experimental data which served as the only means of testing the method. The physical model of separation adopted for the present work, and the application of results from triple-deck theory to obtain a new scaling law for separation length, are described in Sec. IV. A framework developed for describing real-gas effects on separation length is presented in Sec. V, where individual mechanisms are investigated independently of each other by use of various methods.

II. EXPERIMENTAL METHODS

The T5 Hypervelocity Shock Tunnel at Caltech was used to produce short-duration ($\simeq$1 ms), high-speed flows of high stagnation enthalpy ($h_0 > 20$ MJ/kg). A double-wedge test geometry was chosen because it allows greater control over local flow conditions at separation, and at high incidence, may cause significant dissociation downstream of the leading shock. A two-dimensional geometry, as opposed to an axi-

TABLE I. Nominal reservoir and free-stream conditions for the present study. The Reynolds number Re_∞ is based on $L_h = 10$ cm, α is atomic mass fraction, and T_v is a temperature characterizing vibrational excitation.

	h_0 (MJ/kg)	p_0 (MPa)	A_e/A_*	M_∞	Re_{∞,L_h} ($\times 10^5$)	α_∞	T_∞ (K)	T_{v_∞} (K)	ρ_∞ (kg/m^3)	u_∞ (km/s)	p_∞ (kPa)
A1	3.9	12	100	6.8	4.5	$<10^{-3}$	340	2200	0.034	2.5	5.4
A2	4.9	39	100	6.6	11	$<10^{-3}$	450	2100	0.087	2.9	20
			225	7.9	7.3	$<10^{-3}$	330	2200	0.048	2.9	8.1
			400	9.0	5.3	$<10^{-3}$	260	2300	0.029	3.0	4.1
B1	7.0	6.3	100	6.5	1.1	0.0014	680	3000	0.0098	3.4	4.1
			225	7.8	0.87	$<10^{-3}$	450	3100	0.0059	3.4	1.2
			400	8.8	0.62	$<10^{-3}$	380	3200	0.0037	3.5	0.72
B2	8.3	20	100	6.3	2.8	0.0013	840	2800	0.026	3.7	12
			225	7.6	2.0	0.0015	590	2900	0.015	3.8	3.8
			400	8.6	1.5	0.0015	470	3000	0.0094	3.8	2.3
B3	11	57	400	8.2	3.2	0.0016	670	3000	0.023	4.3	7.1
C1	21	28	400	7.2	0.81	0.059	1300	3900	0.0070	5.6	4.1
C2	24	17	100	5.0	0.73	0.11	2700	4000	0.011	5.7	12
			225	6.3	0.61	0.11	1800	4100	0.0065	5.8	6.8
			400	7.3	0.48	0.12	1400	4200	0.0041	5.9	2.5
C4	28	23	100	4.8	0.83	0.13	3200	4100	0.013	6.0	17
			225	6.0	0.63	0.15	2200	4200	0.0073	6.2	11
			400	7.0	0.57	0.15	1700	4300	0.0052	6.3	8.1

symmetric double cone, was selected because it allows easy adjustment of θ_1 and θ_w without separate realizations of the hardware, and provides increased sensitivity of line-integrated flow visualization techniques. The disadvantage of a double-wedge configuration is that the flow is inherently three dimensional; this is addressed in Sec. II D 2. Separation length was measured using flow visualization, and the test model was instrumented to measure heat flux and static pressure.

A. Flow conditions

The T5 Hypervelocity Shock Tunnel uses a free piston, driven by compressed air, to adiabatically compress the driver gas of a shock tube, the reflected shock region of the shock tube then acting as the reservoir for a nozzle expansion to the desired flow conditions. The operation and performance of this facility are described elsewhere.[49–51] The present investigation used a conical nozzle of 7° half-angle and 30 cm exit diameter, with three interchangeable throat sections providing nozzle exit area ratios (A_e/A_*) of 100, 225, and 400. The local conditions at separation were controlled by varying the reservoir conditions (pressure p_0 and enthalpy h_0), A_e/A_* and θ_1. Experiments were limited to nitrogen test gas. The reservoir conditions were labeled A1–2, B1–3, and C1–4 according to h_0, and are presented in Table I along with the free-stream conditions for each A_e/A_* used in this study.

Reservoir pressure p_0 was measured with $\pm 5\%$ accuracy, and h_0 was estimated, from p_0 and the measured speed of the incident shock, using a standard technique.[52] A single-shot uncertainty of $\pm 8\%$ in h_0 was assumed. The values in Table I are averaged over all experiments at each condition. The shot-to-shot variability was as high as $\pm 10\%$ in h_0 and $\pm 15\%$ in p_0 for some conditions, but was not an issue because experiments were analyzed individually.

The free-stream conditions were computed for each experiment using the method described in Sec. III B. The values in Table I were taken from the nozzle centerline at the nozzle exit plane and averaged over all experiments at each condition. Uncertainty in the computed free-stream conditions due to uncertainty in the reservoir conditions was estimated by recomputing one high-enthalpy case with modified h_0 and p_0, which gave $\pm 6\%$ in p_∞, $\pm 7.8\%$ in ρ_∞, $\pm 5.6\%$ in T_∞, $\pm 3\%$ in u_∞, $\pm 20\%$ in α_∞, and $\pm 1.6\%$ in T_{v_∞}.

B. Test model

The double-wedge model consisted of a forward plate (20.32 cm span $\times$ 10.16 cm chord) followed by a full-span trailing flap (5.08 cm chord). Flap deflection angles $\theta_w = 5° - 40°$ in 5° increments were obtained by use of keyed positioning wedges. The incidence angle of the assembly was adjustable to $\theta_1 = 15°$, 30°, 35°, and 40°. Vertical translation of the model maintained constant vertical position of the leading edge while varying θ_1. The housing underneath the front plate was sloped to ensure an attached leading-edge shock. The leading edge remained sharp with radius stabilized at approximately 100 μm, and was removable for repair. The wetted surfaces were made of stainless steel. Figure 2 shows a view of the test model installed in T5.

The vertical and streamwise horizontal position of the model relative to the nozzle were both measured to about ± 1 mm accuracy, the latter by recording the shock tunnel recoil motion during each experiment. In the spanwise horizontal direction, the model was offset approximately 7 mm from the nozzle centerline due to permanent mounting rail misalignment. The model was aligned to gravity about its pitch and roll axes, but yaw axis alignment was not adjustable. Small misalignments at the hingeline often arose due to machining and assembly tolerances, resulting in a slight step of less than 40 μm, or in a some cases a slight gap of less than 25 μm, at one end of the hingeline. Hingeline steps have

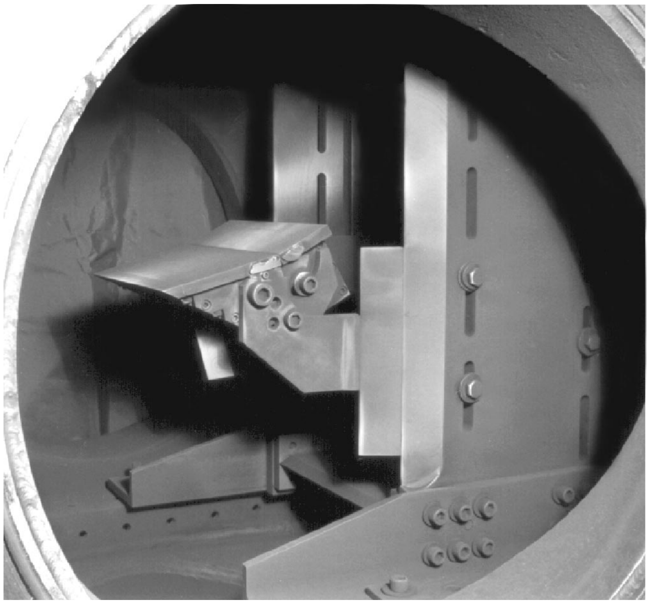

FIG. 2. View of the double-wedge test model installed in T5.

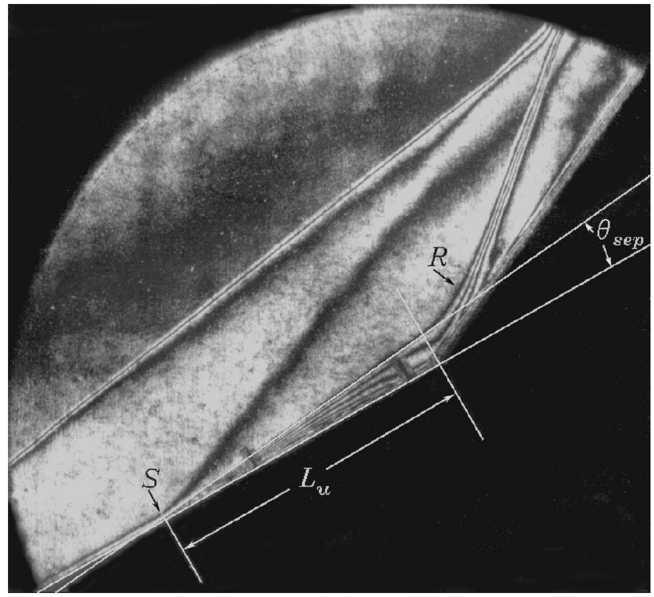

FIG. 3. Example interferogram showing measurement of L_u and θ_{sep} (condition C2, $A_e/A_* = 225$, $\theta_1 = 30°$, $\theta_w = 25°$).

been shown to simply shift the effective corner location,[53] and hingeline gaps of this size have been shown to have negligible effect on L_{sep} for high Mach-number interactions[54] but may be of significance for the low Mach-number interactions found at $\theta_1 > 30°$ in the present experiments.

C. Diagnostics

1. Flow visualization

Flow visualization offered the most accurate means of measuring separation length. The primary technique was holographic interferometry, with some use also of shadowgraphy. Both techniques relied on a Nd:YAG laser light source (frequency doubled to 532 nm wavelength) with duration on the order of 2 ns to effectively ''freeze'' the high-speed flow field. An interference filter blocked broadband emission from high-temperature regions of the flow, and a digital controller fired the laser at a predetermined time, t_{las}, after shock reflection in the nozzle reservoir.

The holographic interferometer built by Sanderson[38] was used to obtain the equivalent of infinite-fringe Mach–Zehnder interferograms by recording two holograms of the object beam, before and during the flow, on the same piece of film and reconstructing them simultaneously. This device has a 7 cm field of view, and could be used in single-pulse mode for shadowgraphy. Two pins were mounted on the side of the model to provide a length scale. For some experiments, shadowgraphy was performed using a conventional single-pass folded-Z optical system with a 20 cm field of view.

An example interferogram is presented in Fig. 3 to illustrate the method for measuring L_{sep}. Because the reattachment location R could not be assessed with any accuracy, L_{sep} was measured indirectly by measuring L_u and θ_{sep}, with L_{sep} given by the geometry in Fig. 1. Subjectivity was accounted for by assigning uncertainties to the measurements. The algorithm for measuring L_u and θ_{sep} was confirmed by comparison to interferograms computed from two-dimensional viscous double-wedge flow simulations. These computations also showed that the dividing streamline ψ^* is generally curved at S and R, and that the criterion of vanishing wall shear stress can give a result for L_{sep} significantly different from the interferometric measurement.[55]

2. Instrumentation

Heat flux was measured using coaxial type E (constantan–chromel) surface thermocouples, designed originally by Sanderson,[38] with response times on the order of 1 μs. Amplified voltage signals from each thermocouple were digitally sampled at 200 kHz and converted to surface temperature signals assuming a reference junction at ambient temperature. Time-resolved heat flux $\dot{q}$ was obtained by a spectral deconvolution method based on the theory of one-dimensional heat conduction in a semi-infinite slab. Given some estimate of the noise spectrum, this method provides optimal filtering. In the present study, a low-pass square cut-off filter was used to remove all high-frequency components above 20 kHz. The method also requires constant thermal properties; these were estimated by averaging constantan and chromel thermal property data from Sundqvist,[56] evaluated separately for each signal at the average measured temperature between the time of initial temperature rise and the time t_{las} of flow visualization.

Spatial heat flux distributions were obtained by averaging each $\dot{q}$ signal over a 100 μs time period centered on t_{las}. An uncertainty was estimated for each measurement by combining the following three sources of error: (1) ±1.7% based on standard tolerance of the voltage-to-temperature conversion; (2) ±8% based on uncertainty in thermal property data[56] and comparison to limited calibration results; (3) uncertainty due to unsteadiness taken as twice the standard deviation of the $\dot{q}$ signal over the averaging period. Along the model centerline were arrayed 27 thermocouple ports, 17 of these upstream of the hingeline. Additional ports were placed at outboard spanwise positions.

Limited pressure measurements were taken using PCB 105B12 miniature piezoelectric transducers. These were mounted in a recessed configuration (with 0.8-mm-diam tapping) designed to protect the gauge head from the harsh flow environment while maintaining a reasonable response time to the initial flow starting process and avoiding cavity resonance. Improved signal-to-noise ratio was obtained by filling the mounting thread with silicone sealant to provide vibrational damping. Voltage signals were sampled and processed in a similar fashion to the heat flux measurements, with the spectral method used for filtering, and the conversion to pressure based on individually calibrated sensitivities. Uncertainties were estimated from unsteadiness during the averaging period and uncertainties in calibration. The model is furnished with a staggered streamwise array of 10 transducer ports slightly offset from the centerline, 6 of these upstream of the hingeline, and 4 additional ports at outboard spanwise positions. Some streamwise heat flux and pressure distributions are presented in Sec. III C to test computational methods.

D. Flow quality

1. Test time, disturbances, and unsteadiness

One major concern in shock tunnel experiments is the limited test time available, especially at high enthalpy. Conservative estimates were made for the time required to establish steady separated flow, with the time for nozzle starting measured from heat flux signals and the time for separated flow establishment calculated from various existing criteria.[57] For all the present conditions, these estimates indicated flow establishment well in advance of the time t_{las} at which flow visualization was performed. The model of Davies and Wilson[58] was used to estimate the time at which driver-gas contamination commences. This model has shown good agreement with experimental results for T5 under nominally tailored interface conditions.[59] The degree of off-tailoring has a large effect on the arrival time t_{dgc} of driver gas at medium and high enthalpy (but not low enthalpy), with t_{dgc} advanced by overtailoring and delayed by undertailoring.[60,61] Condition C4 was consistently overtailored and expected to suffer significant contamination by time t_{las}. Condition C2, only marginally contaminated for a tailored interface, was consistently undertailored and thus expected to suffer contamination of no more than a few percent until several hundred microseconds after t_{las}. Estimates for all other conditions indicated no contamination by time t_{las}.

Heat flux distributions from two experiments with $A_e/A_* = 100$ and the model leading edge either above or below the nozzle centerline showed no effect that could be attributed to stationary disturbances in the nozzle flow. Acoustic disturbances to the free-stream flow were not investigated. A number of experimental configurations gave a total deflection angle $\theta_1 + \theta_w$ greater than the maximum deflection angle, resulting in strong shock–shock interaction between the leading-edge shock and the reattachment shock. The pattern typically observed involved impingement of a jet-like structure on the flap downstream of reattachment, producing large peaks in heat flux and pressure. The existence of such an interaction did not hinder measurement of L_{sep} as long as reattachment occurred upstream of the interaction's region of influence.

The experimental flow field was inherently unsteady due to disturbances generated by piston motion in the shock tube driver and to nonuniformities in the reflected shock region. Correlated large-scale unsteadiness was often observed in heat flux signals well after the expected flow establishment time, for the locations of separation and, in cases with strong shock–shock interaction, jet impingement. The latter was not of concern because it did not influence reattachment. Temporal variations in the separation location were within experimental error bounds on separation length measurement. In general, as long as variations in the flow properties were small compared to their mean values over some period about t_{las}, then the mean flow was assumed to closely resemble a truly steady flow of the same mean flow properties.

2. Three dimensionality

The use of a finite-span configuration and a conically diverging free stream produced an inherently three-dimensional flow field. Analysis and computations, however, must rely on the assumption of two-dimensional flow to obtain results with reasonable effort. Ideally, this would require that the flow field within a vertical plane near the centerline of the model remains independent of spanwise location. The experiments could not attain this ideal, but did offer a reasonable approximation that allowed two-dimensional analysis to illuminate important results in the data relevant to separation length.

Common methods for minimizing end effects due to finite model span are to add side fences to prevent spillage or increase span until the centerline flow is independent of aspect ratio. The addition of side fences to models of low aspect ratio invariably increases separation length,[11,22,25,62] which, though consistent with the idea that they prevent spillage, is in fact due to interaction with the corner formed by the fences; Kornilov[63] showed by shock-impingement experiments in a variable-width channel that sidewalls significantly increase L_{sep} for a span $b \lesssim 85\delta$, where δ is the thickness an undisturbed boundary layer would have at the hingeline, while Hankey and Holden[64] found that the addition of side fences to a model of aspect ratio AR$=0.5$ increased L_{sep} beyond the nominally two-dimensional value found for AR$=1$. The extent of end effects without side fences should also depend on boundary-layer thickness. Ball[65] studied a large-span flat plate with a trailing flap of varying span and found that three dimensionality as evidenced in the separation length encroached only a distance of $10\delta_1$ from the sides of the flap, where δ_1 is the boundary-layer thickness at separation. The ratio b/δ_1 was on the order of 100–200 for the present work, and thus additional experiments with side fences or increased span were deemed unnecessary.

Spanwise measurements of pressure, and of heat flux downstream of reattachment, showed no consistent behavior. Upstream of separation, a slight increase in heat flux with distance from the centerline was found throughout the experiments but could not be explained. Lewis *et al.*[26] showed that uniform spanwise distributions are a necessary but insufficient condition for two dimensionality. The scatter in heat flux measurements downstream of reattachment may be due in part to three-dimensional instabilities in the form of streamwise Görtler vortices, which have been observed experimentally under many supersonic and hypersonic conditions,[11,31,66,67] and can cause variations in heat flux up to 50% of the mean value.[31] A striation pattern typical of this phenomenon was observed in the soot left on the model after some experiments with large θ_w.

Though the model span was sufficient to produce two-dimensional flow on the model centerline for a two-dimensional incoming free stream, the real free stream was three dimensional due to the finite extent and conical divergence of the undisturbed nozzle core flow. For configurations at the highest incidence, a Mach cone emanating from the nozzle exit lip interfered with the double-wedge flow field only at the outboard edges of the trailing flap. Comparison to a control experiment using the T5 contoured nozzle under conditions which produce parallel exit flow showed no effect on the shape of spanwise heat flux distributions due to flow divergence, but a significant effect in the streamwise direction due to axial gradients. The conical free stream was approximately accounted for in analysis, as described in Sec. III B.

III. COMPUTATIONAL METHODS

The present study relies on an advanced computational technique because many flow parameters of interest could not be measured experimentally, nor could they be predicted with reasonable accuracy by simple analysis due to the nonuniform, nonequilibrium nature of the flow.

A. Nonequilibrium Navier–Stokes code

The computer code, obtained from Olejniczak[68] and based on the work of Candler,[69] solved a finite-volume representation of the Reynolds-averaged Navier–Stokes equations including thermochemical nonequilibrium. The code simulated only two-dimensional (planar or axisymmetric) flows of nitrogen. Rotational internal energy modes were assumed to be in equilibrium with translational modes, but vibrational modes were considered separable and characterized by a vibrational temperature T_v. Electronic excitation and ionization were neglected. The code used a simple harmonic oscillator model for vibrational energy, and a simplified version of the Bartlett *et al.*[70] model for diffusion. Viscosity and thermal conductivity were computed using the mixing rules of Gupta *et al.*,[71] and vibrational relaxation was modeled using the Landau–Teller formulation with semi-empirical results from Millikan and White.[72] An Arrhenius form was assumed for dissociation rates, with a modified temperature according to the Park[73] vibration–dissociation coupling model, and constants from Park.[74] Recombination rates were then obtained from a curve fit[71] to the equilibrium constant. All viscous calculations are laminar; the code did not include turbulence models.

The vectorized, discretized conservation equations were solved on a body-fitted numerical grid with generally non-Cartesian coordinates ξ (the streamwise direction) and η (the body-normal direction). The technique used upwind differencing with modified Steger–Warming flux splitting,[75] which captures shocks well but is modified in viscous shear regions to avoid excess numerical dissipation. A steady-state solution was obtained by Gauss–Seidel line relaxation, a fully implicit iterative technique in which block-tridiagonal matrix inversion is applied to individual η-gridlines during backward and forward sweeps in the ξ direction.

Supersonic inflow boundaries were held fixed at their initial values, and supersonic outflow boundaries were handled by zero-gradient extrapolation. Inviscid wall or symmetry boundaries had zero normal pressure gradient and zero normal fluxes. At viscous wall boundaries, the additional constraints of zero velocity and constant temperature (300 K, in equilibrium with vibrational temperature) were applied. The viscous wall condition for species concentration could be selected as either fully noncatalytic (zero normal gradient) or fully catalytic (zero atomic mass fraction). Further details on the computational code are given elsewhere.[55,68,69]

B. Procedure for simulating experiments

For each experiment, computations were performed to estimate external flow parameters at separation and reattachment. Starting with the nozzle reservoir conditions, a quasi-one-dimensional equilibrium flow was computed to a short distance downstream of the throat, the result then used to initialize the inflow boundary of an axisymmetric, nonequilibrium nozzle-flow computation. The latter employed a grid of 200×100 cells, clustered at the upstream and wall boundaries, and extending beyond the real nozzle exit to encompass the double-wedge model. Wall clustering was adequate for prediction of displacement effects but not wall fluxes. Resolution in the axial direction was assumed to be more than adequate for producing a grid-converged solution of a simple inviscid expanding core flow. The laminar computation only approximately accounted for displacement effects; the real nozzle boundary layer is transitional or turbulent. The technique also neglected deviation of the nozzle wall near the minimum area from a conical profile. Subsequent wedge-flow computations were initialized using parabolic fits to nozzle-flow results along the centerline downstream of the nozzle exit, assuming purely conical free-stream flow and accounting for the measured position of the model. Initialization of planar wedge computations by an axisymmetric free-stream expansion introduced error into the steady-state wedge-flow solutions, shown to be on the order of 3% in p, 2% in ρ, and <1% in T just upstream of the leading shock.

External flow parameters were estimated by computing inviscid flow on a triple-wedge geometry, where an impermeable straight-line boundary between S and R replaced the experimentally measured separation region; an example is shown in Fig. 4. The grids consisted of 220×100 cells dis-

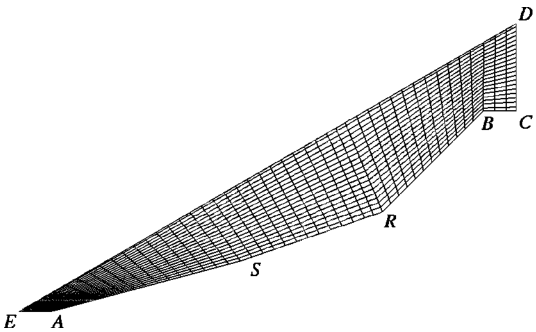

FIG. 4. Example of finite-volume grid for inviscid triple-wedge computations (every fifth gridline is shown).

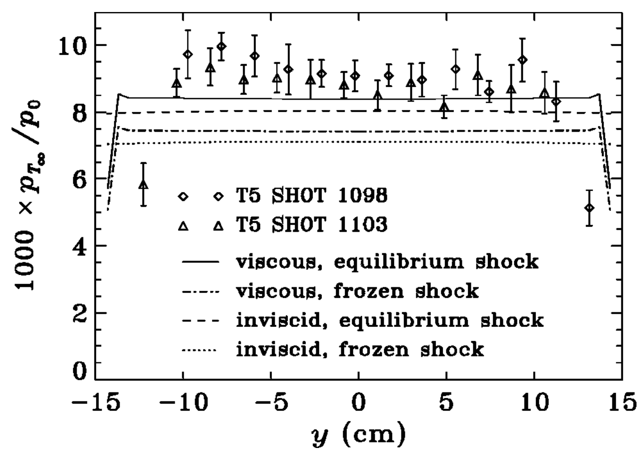

FIG. 5. Comparison between measured [(◇) and (△) for two shots at nominally the same condition] and computed (various curves as indicated) free-stream pitot pressure for a high-enthalpy condition ($h_0 \simeq 25$ MJ/kg, $p_0 \simeq 21$ MPa, $A_e/A_* = 225$). Calculated distributions are based on a limited number of data extracted from computational results, and thus appear to have low spatial resolution. Error bars include only standard deviation of pressure time history over averaging period, and y is the distance above nozzle centerline (model is located in $y > 0$ cm).

tributed uniformly. These were shown by a grid-convergence study to provide a converged solution in the region of interest, adjacent to the wall but away from shocks. A grid of 275×125 cells resulted in narrower numerical overshoots at shocks, but an otherwise identical solution. A trailing-edge expansion assured supersonic outflow. The symmetry condition applied along EA in Fig. 4 is unphysical when the leading edge is vertically displaced from the nozzle centerline, but this was shown, by comparison to results from grids wrapped around the leading edge, to have negligible effect on the flow properties of interest. The viscous–inviscid interaction neglected in these computations was shown by comparison to viscous computations to be negligible for $\theta_1 \geqslant 30°$ and cause no more than 5% errors in edge-flow properties for $\theta_1 = 15°$. External flow parameters were extracted from the inviscid computations for stations 1 and 2 just upstream of the pressure rise at separation and reattachment, respectively, and for station 3 at a consistently defined location downstream of reattachment based on the numerical overshoot found for a uniform free stream.

Steady-state solutions for cases with strong shock–shock interaction typically overestimated the upper-shock standoff distance, consistent with an experimentally observed upstream motion of jet impingement, though it should be emphasized that the computational code was not time accurate. Other possible causes for the discrepancy were eliminated, suggesting that a global steady state had indeed not been established in these experiments. In such cases, the computation was halted when the interaction pattern approximately matched experiment and the solution had locally reached a steady state in the region of interest, along the wall past reattachment.

C. Comparisons to experiment

Many comparisons were made between computational results and surface measurements from the present experiments, because previous testing of the code for attached wedge flows was very limited.[68] Some results are presented here for each type of computation undertaken.

1. Nozzle-flow computations

The only nozzle-flow measurements available for T5 are those taken using a rake of pitot pressure probes. Because pitot pressure is insensitive to the thermochemical state of the gas, such measurements cannot validate the thermochemical models used in the code; they can only verify that the code reproduces the overall fluid mechanics. Nozzle-flow computations were performed at a high-enthalpy test condition from a previous experimental study in T5 for which free-stream pitot surveys of the conical nozzle had been undertaken.[41] Both viscous and inviscid computations were considered, in order to ascertain the boundary-layer displacement effect. Using the free-stream properties predicted by the code, pressure downstream of a normal shock was calculated under the limiting assumptions of frozen and equilibrium flow. Results are shown in Fig. 5, with the pitot pressure p_{T_∞} normalized by the reservoir pressure.

The viscous-flow computation with equilibrium-shock assumption falls closest to the experimental data, but still slightly lower, suggesting that a laminar assumption only partially accounts for the boundary-layer displacement effect. It is not clear by how much the present method underpredicts free-stream pressure in general; the ±5% uncertainty in p_0 is not included in Fig. 5, Olejniczak[68] found good agreement for a high-enthalpy condition assuming laminar flow and a frozen shock, and pitot probe results from the contoured nozzle at the HEG shock tunnel match turbulent calculations at low pressure but laminar calculations at high pressure.[76] The measurements in Fig. 5 also show a slight lobe-like nonuniformity.

2. Inviscid triple-wedge computations

Two comparisons are presented in Fig. 6 between experimental measurements and inviscid computational results for the pressure coefficient. The agreement near separation in Fig. 6(a) is rare; pressure measurements for $x < L_h$ typically have large scatter and uncertainty. In the flap region downstream of reattachment, there is a tendency for the computation to underpredict the pressure as shown in Fig. 6(a), but

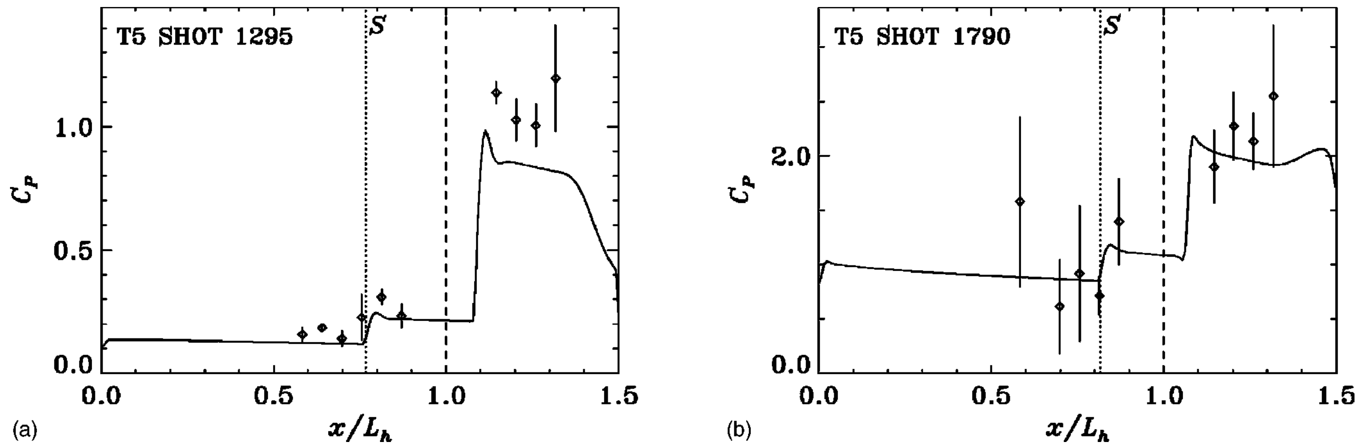

FIG. 6. Two comparisons between experimental pressure measurements (◇) and inviscid triple-wedge computational results (solid curve) for (a) T5 shot 1295 (condition B3, $A_e/A_* = 400$, $\theta_1 = 15°$, $\theta_w = 20°$) and (b) T5 shot 1790 (condition C2, $A_e/A_* = 100$, $\theta_1 = 40°$, $\theta_w = 20°$). The dashed line is hingeline location, the dotted line is the separation location measured from flow visualization, and $C_P = 2p/\rho_\infty u_\infty^2$. Error bars are described in Sec. II C 2. Overshoots at separation and reattachment are numerical, not physical.

this behavior was not found consistently throughout all cases computed. For example, in Fig. 6(b) the computed pressure approximately matches experiment at reattachment, but is too low further downstream where the computation fails to reproduce the experimental location of jet impingement from a strong shock–shock interaction.

The following five mechanisms were identified as possible causes of error in computed flap pressure: (1) incorrect free-stream pressure due either to uncertainty in p_0 or laminar nozzle boundary-layer assumption; (2) neglected or incorrect free-stream nonuniformity due to nozzle wall disturbances or the planar-axisymmetric initialization problem mentioned in Sec. III B; (3) neglected viscous–inviscid interaction effect when $\theta_1 = 15°$ (4) neglected boundary-layer transition near reattachment in some cases, previously shown to have an important effect on the pressure distribution;[77] (5) large uncertainty in the measured separation angle θ_{sep}, on which the exact geometry of triple-wedge computations depends. Each mechanism may have different trends depending on the flow condition, and with the large scatter in experimental pressure measurements, it is not surprising that there is little consistency in comparisons of the computed flap pressure results to experiment. Comparisons between measured and computed shock angles[55] show good agreement for the leading shock but some discrepancies for the reattachment shock.

3. Single-wedge computations

A few viscous computations were performed on single-wedge geometries to ascertain the magnitude of viscous interaction effects (see Sec. III B) and to verify the code's ability to reproduce experimentally measured heat flux. The grids consisted of 218×100 cells, clustered at and wrapped around the leading edge. The grids were clustered at the wall to provide well-resolved boundary-layer solutions with 35 cells inside the displacement thickness estimated from frozen-flow theory.[55] These computations are very similar to the boundary-layer computations described in Sec. V B 1, for which both grid resolution in the transverse direction and grid dependence on leading-edge refinement are considered. Inviscid computations, without wall clustering, were also performed; grid convergence in this case is proven by results for the inviscid triple-wedge computations (see Sec. III B).

Results are shown in Fig. 7 for two experiments conducted with $\theta_w = 0°$. Heat flux is made nondimensional using a Stanton number based on free-stream conditions,

$$\mathrm{St}_\infty = \frac{\dot{q}}{\rho_\infty u_\infty (h_0 - c_{p_\infty} T_w)}, \tag{1}$$

where $\dot{q}$ is the heat flux to the wall, T_w is the wall temperature (300 K), and vibrational excitation is ignored when computing c_{p_∞} since it is negligible at the wall.

In addition to experimental measurements and viscous computational results, curves are presented in Fig. 7 for laminar, frozen-flow, flat-plate boundary-layer theory applied to the corresponding inviscid computational solution along the wall, under the assumption of local similarity. These are given to justify the use of this theory later in Sec. IV C. The heat flux was found from the Stanton number definition and Reynolds analogy,

$$\mathrm{St} = \frac{\dot{q}}{\rho_e u_e (h_e + r u_e^2/2 - h_w)} \simeq \frac{C_f}{2\,\mathrm{Pr}^{2/3}}, \tag{2}$$

where Pr is the Prandtl number and $h_e + r u_e^2/2 = h_{aw}$ is the adiabatic wall enthalpy based on the recovery factor $r \simeq \sqrt{\mathrm{Pr}}$ for laminar flow (the subscripts w and e refer, respectively, to the wall and boundary-layer edge). The skin friction coefficient, $C_f = 2\tau_w/\rho_e u_e^2$, was found from the Blasius solution modified by the reference-temperature method,

$$C_f = 0.664\sqrt{\frac{C^*}{\mathrm{Re}_x}}, \tag{3}$$

where C^* is the Chapman–Rubesin parameter $\rho\mu/\rho_e\mu_e$ evaluated at a reference temperature T^* computed from the generalized formula[78]

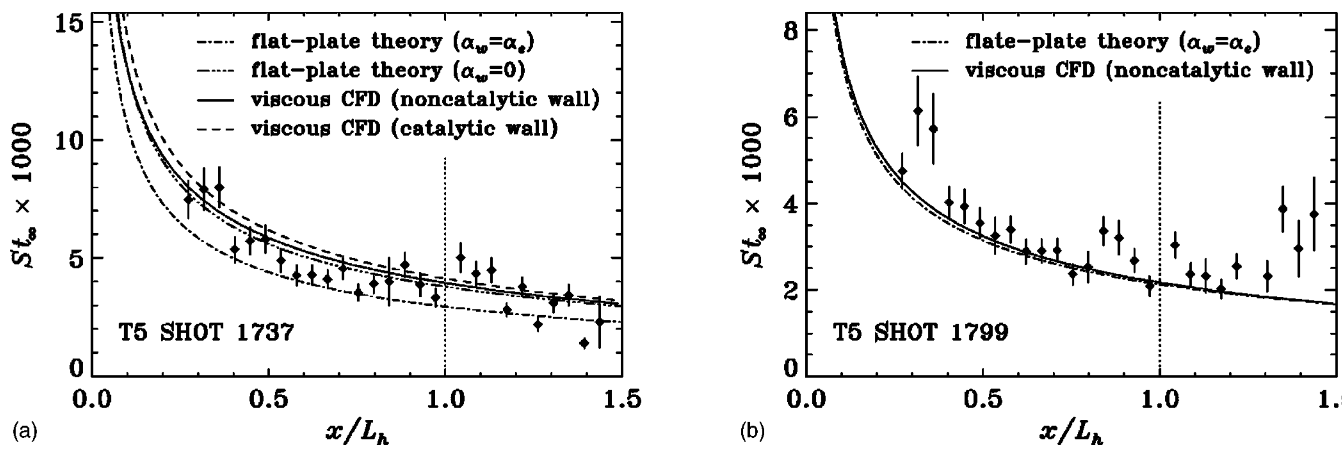

FIG. 7. Two comparisons between experimental heat flux measurements (♦), viscous single-wedge computational results (—noncatalytic; ---catalytic), and flat-plate theory applied to inviscid single-wedge computational results ($\cdot\cdot\cdot\alpha_w=\alpha_e$; $-\cdot\cdot\cdot\alpha_w=0$), for (a) T5 shot 1737 (condition C2, $A_e/A_*=100$, $\theta_1=30°$, $\theta_w=0°$) and (b) T5 shot 1799 (condition B2, $A_e/A_*=100$, $\theta_1=30°$, $\theta_w=0°$). The dotted line is hingeline location, St_∞ is defined by Eq. (1), and error bars are described in Sec. II C 2.

$$\frac{T^*}{T_e}=\frac{1}{2}\left(1+\frac{T_w}{T_e}\right)+\frac{(\gamma-1)\sqrt{\mathrm{Pr}}}{12}M_e^2. \tag{4}$$

The ratio of specific heats γ was evaluated for a dissociated, vibrationally excited gas using

$$\gamma=1+\frac{R}{c_v+(1-\alpha)c_{v_v}}, \tag{5}$$

where the gas constant R and the translational–rotational specific heat capacity c_v are mass averaged over the gas mixture and the vibrational specific heat capacity c_{v_v} of N_2 is evaluated from the simple harmonic oscillator model. Viscosity was estimated using the curve fits of Blottner[79] and mixing rule of Wilke.[80]

For the high-enthalpy case in Fig. 7(a), flat-plate theory results are shown for two different limiting assumptions used to evaluate h_w in Eq. (2). The assumption $\alpha_w=\alpha_e$ corresponds to a truly frozen boundary layer with constant composition, while the assumption $\alpha_w=0$ approximates a reacting flow with full recombination at the wall by considering the difference in chemical enthalpy across the layer but neglecting diffusion. Viscous computational results are shown in Fig. 7(a) for both catalytic and noncatalytic wall boundaries; these are not much different because the gas-phase reaction rates are high enough under this condition to produce strong recombination near the wall regardless of catalyticity. Results from a lower-density condition with $\theta_1=15°$ (not shown) gave a significant difference between catalytic and noncatalytic walls, with experimental data falling between. The test model surface of dirty stainless steel is not expected to be catalytic to nitrogen recombination, which, taken together with the result in Fig. 7(a) that frozen-flow theory slightly underpredicts experiment while reacting-flow computations tend to overpredict experiment, suggests that the reaction rates may be too high in the computations. In other words, the noncatalytic computational result in Fig. 7(a) predicts α_w lower than the real flow. On the other hand, the differences are not much larger than the experimental scatter.

For the low-enthalpy condition in Fig. 7(b), both computation and theory show good agreement with experiment, at least over the middle part of the first wedge. It is clear from the repeatable scatter in experimental data that the heat flux measurements include systematic error not accounted for in the error bars, which might be reduced by calibration of individual thermocouples.

4. Viscous double-wedge computations

Viscous computations were performed for a few conditions using double-wedge geometries to study the relationship between interferometric fringes and other criteria for defining separation. These were also useful for comparisons to measured heat flux downstream of reattachment. Double-wedge grids consisted of 400×200 cells distributed uniformly in the streamwise direction but clustered at the wall with 25 cells inside the displacement thickness estimated from frozen-flow theory.[55]

Critical review of the existing literature on numerical results revealed that accurate computation of separation length in corner flows remains an unresolved problem even for nonreacting flows. Though not a major concern of the present work, this fact is worth expounding upon because it is not generally appreciated in the literature. Computations often underpredict the length of separation,[16,81–84] but some authors report predictions that both underestimate and overestimate experimental L_{sep} depending on the numerical grid or depending on the experiment simulated.[85–88] Though it has been noted that the computed position of separation generally moves upstream with increased grid resolution,[89] both Grasso *et al.*[86] and Rizzetta and Mach[87] have clearly demonstrated that the solution depends not just on the overall grid resolution, as characterized by the number of cells in each spatial direction, but also on exactly how those cells are distributed. Results can be extremely sensitive to such parameters as the spatial distribution of cells in the interaction region, and the aspect ratio of cells at the leading edge, at separation, and at reattachment. One common problem is that grids are refined near the leading edge and near the

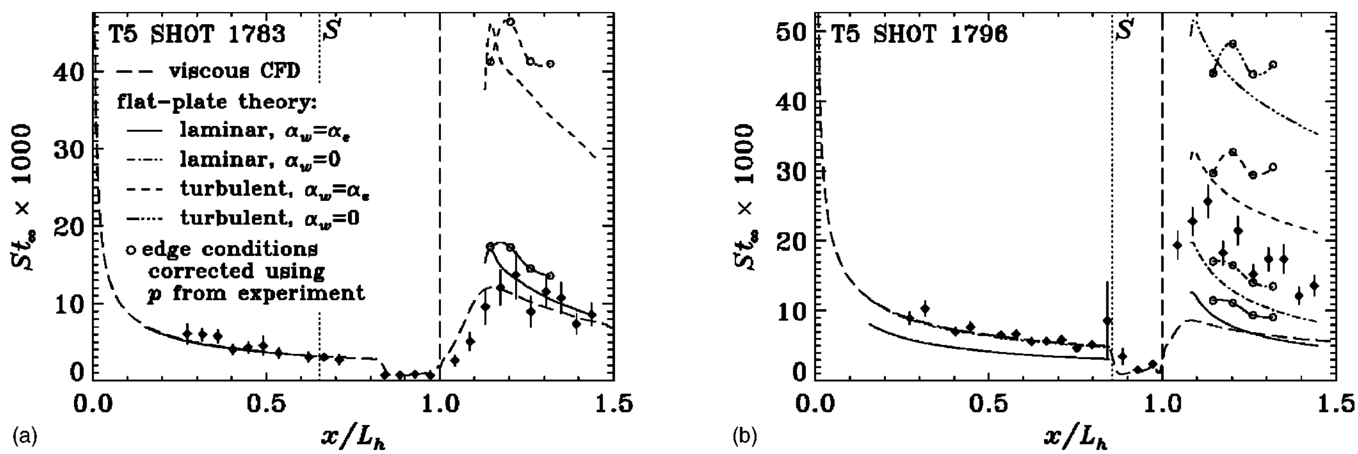

FIG. 8. Two comparisons between experimental heat flux measurements (♦), viscous double-wedge computational results with noncatalytic wall (– – –), and flat-plate theory applied to inviscid triple-wedge computational results (various curves and symbols as indicated), for (a) T5 shot 1783 (condition B1, $A_e/A_*=225$, $\theta_1=15°$, $\theta_w=20°$) and (b) T5 shot 1796 (condition C2, $A_e/A_*=100$, $\theta_1=40°$, $\theta_w=15°$). The dashed line is the hingeline location, the dotted line is the separation location measured from flow visualization, St_∞ is defined by Eq. (1), and error bars are described in Sec. II C 2.

corner, but in well-separated flow, the steady-state separation point is located in between. Rizzetta and Mach[87] also showed large differences between results obtained using different numerical methods. In fact, the different methods exhibited different dependencies on the grid cell distribution. To make matters even worse, some of the experiments commonly used for comparison utilize wind tunnel models of aspect ratio less than unity,[31,90] for which centerline measurements are not necessarily free from three-dimensional flow (see Sec. II D 2). Rudy *et al.*[91] could only obtain good agreement with experiment for a well-separated compression-corner flow by computing the full three-dimensional solution, but Lee and Lewis[92] were able to match the same experimental data using a two-dimensional method. Grid convergence was not studied for the present computations, which were not expected to match experimental separation length but were expected to incorporate the relevant physics of separated flow. The agreement in separation location between computation and experiment in Fig. 8(b) is probably coincidental.

Along with the experimental and viscous computational results in Fig. 8 are presented several flat-plate boundary-layer predictions based on the inviscid solution from triple-wedge computations. Comparison of experimental heat flux downstream of reattachment to laminar and turbulent predictions aided in identifying transitional interactions (see Sec. VI B). Laminar predictions upstream of *S* and downstream of *R* were computed according to Eqs. (2)–(4). Turbulent predictions downstream of *R* were computed using the model of White and Christoph.[93] For the high-enthalpy case in Fig. 8(b), both predictions were computed a second time using the $\alpha_w = 0$ assumption. Downstream of *R*, all predictions were computed yet again using inviscid solutions corrected to match experimental pressure measurements. Corrections to the density and temperature were related to the pressure correction by linearizing the perfect-gas shock jump equations about the upstream state in region 2. A reasonable approximation over the present range of conditions was found to be

$$\frac{\Delta\rho}{\rho}=\frac{\Delta T}{T}=\frac{1}{2}\frac{\Delta p}{p}. \tag{6}$$

Velocity was not corrected. The open circles in Fig. 8 indicate the transducer port locations. All predictions downstream of *R* were computed with the origin placed at the hingeline to account in a consistent manner for compression of the boundary layer at reattachment.

For the low-enthalpy condition in Fig. 8(a), the interaction is clearly a purely laminar one, with experiment, computation, and flat-plate theory all in good agreement. The uncorrected prediction matches experiment better than the corrected prediction in this case, but the opposite was found most often among the present results. For the high-enthalpy condition in Fig. 8(b), the prediction with $\alpha_w=0$ best matches experiment upstream of *S* and is therefore assumed the best prediction downstream of *R*. Experimental heat flux lies much closer to the laminar prediction than to the turbulent prediction with $\alpha_w=0$, suggesting a purely laminar interaction. The pressure-corrected result falls even closer to experiment. The viscous double-wedge computation seriously underpredicts heat flux in the flap region, probably due to poor resolution of the extreme gradients introduced at reattachment by impingement of a shear layer containing hot dissociated gas (see Fig. 18).

IV. ANALYSIS OF SEPARATION LENGTH

A. Physical description of separation

The physical process which determines separation length has been elegantly described by Glick[94] as follows: An element of fluid at *S* just outside the dividing streamline ψ^* has zero velocity and a total pressure p_T equal to the local static pressure p_S, but when this element reaches *R*, it must have $p_T=p_R>p_S$; the mechanical energy increases by viscous transport of momentum from the outer flow toward ψ^*. Thus as θ_w is increased, p_R increases and the separated shear layer requires a longer distance to impart the necessary momentum. There is also a weak coupling between the flow at R and the flow at S; $\theta_{\rm sep}$ depends on the position of S which depends on p_3/p_2, which itself depends on $\theta_{\rm sep}$.

A popular model for the separation bubble due to Chapman *et al.*[95] requires that p_T along ψ^* as it approaches R be equal to the static pressure p_3 downstream of R. The analysis assumes an isentropic compression process along ψ^* close to R, ignores the fact that p_R is lower than p_3, and neglects the initial thickness of the boundary layer at S. While these errors tend to cancel each other for flows with incoming boundary-layer thickness small compared to separation length,[96] the effect of initial thickness has been shown to be important in some cases.[97,98]

The model used in the present work relies on a momentum balance between shear forces acting on ψ^* and the pressure rise at reattachment, an idea due originally to Sychev[99] and applied by Roshko[100] to the problem of separation length in supersonic base flow. This balance can be written

$$\int_0^{y_R}(p_{\psi^*}-p_2)\,dy=\int_{x_1}^{x_R}\tau_{\psi^*}\,dx, \tag{7}$$

where the small shear stress along the wall has been neglected, and the separation geometry of Fig. 1 has been approximated for small $\theta_{\rm sep}$ as an upstream facing step of height y_R equal to the perpendicular distance of R from the first wedge surface. For laminar interactions, p_{ψ^*} is equal to the plateau pressure over much of the separated region, increasing only close to R. Thus $L_{\rm sep}$ is determined largely by the reattachment pressure rise and the evolution of shear stress along ψ^*. This model requires information about the development of the velocity profile in the free-shear layer; the theoretical approach discussed in Sec. IV C relates the shear stress along ψ^* to the wall shear stress of the incoming boundary layer undisturbed by separation.

The length of separation is also very sensitive to the location of transition to turbulence. If transition occurs in the free-shear layer upstream of reattachment, the resulting change in velocity profile increases τ_{ψ^*} and decreases $L_{\rm sep}$ compared to a purely laminar interaction.

B. Previous scaling results

There are relatively few published results concerning the quantitative functional dependence of $L_{\rm sep}$ on relevant flow parameters. Two empirical correlations are considered here: one due to Needham[12] based on experimental data from laminar hypersonic ($7<M_1<15$) compression-corner flows,

$$\frac{L_{\rm sep}}{x_1}\propto\frac{\sqrt{\mathrm{Re}_{x_1}}}{M_1^3}\left(\frac{p_3}{p_2}\right)^2, \tag{8}$$

and one due to Katzer[18] based on numerical data from laminar supersonic ($1<M_1<4$) shock-impingement flows,

$$\frac{L_{\rm sep}}{\delta_1^*}\propto\frac{\sqrt{\mathrm{Re}_{x_1}/C}}{M_1^3}\left(\frac{p_3-p_{\rm inc}}{p_1}\right), \tag{9}$$

where C is the Chapman–Rubesin parameter, $p_{\rm inc}$ is the wedge pressure for incipient separation, and δ_1^* is the displacement thickness an undisturbed boundary layer would have at separation.

Both Eqs. (8) and (9) show an inverse-cubic dependence on M_1, but the dependence on p_3 appears to be different for supersonic and hypersonic interactions. This behavior with M_1 and p_3 was also found by other authors.[36,85,101,102] The dependence on Re_{x_1} in Eq. (8) is consistent with an inverse proportionality between $L_{\rm sep}$ and C_{f,x_1}, as might be expected from Eq. (7) if τ_{ψ^*} scales with C_{f,x_1}. The dependence on Re_{x_1}/C in Eq. (9) arises only from normalization by δ_1^*. There is no consistency in published results for the dependence of $L_{\rm sep}$ on Re_{x_1} or C_f; Eq. (8) is the most convincing because it correlates data from multiple sources over a reasonable range in Re_{x_1}.

Burggraf[103] derived a theoretical scaling law based on asymptotic boundary-layer theory. Katzer[18] recognized this result as having the same Mach-number dependence and same construction of pressure ratio factor as his own empirical result, Eq. (9). He also suggested that asymptotic theory may produce the correct scaling for wall temperature effects on separation length, interpreting Burggraf's result to give $L_{\rm sep}\propto(T_w/T_1)^{3/2}$. No empirical results exist for wall temperature scaling.

C. Application of asymptotic theory

Asymptotic theory has been shown capable of partially reproducing scaling laws found previously by purely empirical methods, not only for separation length as mentioned in Sec. IV B, but also for incipient separation.[104,105] For this reason it was used in the present work to develop a new scaling, applicable to cold nonadiabatic walls, to account for wall temperature effects on separation length.

The present analysis is based on the classical triple-deck formulation of Stewartson and Williams[106] for self-induced separation upstream of an externally enforced disturbance. Flow near separation is considered as a perturbation to the undisturbed incoming boundary layer. Flow variables are expanded in terms of the small parameter $\epsilon=\mathrm{Re}_{x_1}^{-1/8}$ and written in terms of the vertical coordinates $Y_L=\epsilon^{-5}y$ in the lower (viscous, incompressible) deck, $Y_M=\epsilon^{-4}y$ in the middle (inviscid, compressible) deck, and $Y_U=\epsilon^{-3}y$ in the upper (supersonic, isentropic) deck. Perturbations to the energy equation are not considered; the effect of heat transfer enters the problem only through the definition of the undisturbed boundary layer. According to more recent work by Brown *et al.*,[30] the present experimental conditions are well within the supercritical wall temperature range where the classical theory is appropriate. Asymptotic matching between decks reduces the problem to one of solving the lower-deck equations subject to novel boundary conditions. In order to nondimensionalize the lower-deck equations to a canonical form, Stewartson and Williams[106] introduced scaled variables (denoted with a tilde) such as

$$\tilde{x}=\frac{x-x_1}{a\epsilon^3},\quad \tilde{y}=\frac{y}{b\epsilon^5},\quad \tilde{u}=\frac{bu}{d\epsilon}, \tag{10}$$

where the constants a, b, and d are functions of the incoming Mach number M_1, the wall conditions, and the skin friction of the undisturbed boundary layer. For example,

$$a=\left[\frac{M_1^2}{\sqrt{M_1^2-1}}\right]^{3/4}\frac{U_0'(0)^{1/4}}{M_0'(0)^{3/2}}\left(\frac{\epsilon^8}{\nu_w}\right)^{1/4}, \tag{11}$$

where $\nu=\mu/\rho$ is the kinematic viscosity, $U_0(Y_M)$ and $M_0(Y_M)$ are the velocity and Mach-number profiles of the undisturbed boundary layer, and prime denotes differentiation with respect to Y_M.

A five-deck asymptotic structure describing flow downstream of separation was later introduced by Stewartson and Williams[107] and independently by Neiland.[108] For large scaled distance $\tilde{x}$ downstream of separation, a form was found for the flow near ψ^* that asymptotically matches the flow near separation; the leading-order term in the series for scaled velocity is

$$\tilde{u}\sim\tilde{x}^{1/3}F_0'(\tilde{\eta}),\quad \tilde{\eta}=\frac{\tilde{y}-A(\tilde{x})}{\tilde{x}^{1/3}}. \tag{12}$$

A prime denotes differentiation with respect to $\tilde{\eta}$, and the function $A(\tilde{x})$ is linear for large $\tilde{x}$ such that $\tilde{\eta}=0$ corresponds to the dividing streamline.

This asymptotic solution for flow near ψ^* downstream of S is to be applied to the model embodied in Eq. (7), rewritten here as

$$\int_{x_1}^{x_R}\left(\mu\frac{\partial u}{\partial y}\right)_{\psi^*}dx\propto y_R(p_3-p_2). \tag{13}$$

The proportionality implies that p_R scales with p_3, which is not in general true, but (for lack of any better theory for the reattachment process) is assumed to hold approximately under the present conditions. Then using the transformations in Eq. (10), the chain rule for partial derivatives, plus the expressions in Eq. (12), the integrand on the left-hand side of Eq. (13) may be written

$$\left.\frac{\partial u}{\partial y}\right|_{\psi^*}dx\sim\frac{ad}{\epsilon b^2}F_0''(0)d\tilde{x}. \tag{14}$$

Similarly, $y_R=\epsilon^5 b\tilde{x}^{1/3}$. Substituting these into Eq. (13), taking $\mu_{\psi^*}=\mu_w$, and solving for $\tilde{x}_R$ gives

$$\tilde{x}_R\propto\left[\frac{\epsilon^6 b^3(p_3-p_2)}{ad\mu_w F''(0)}\right]^{3/2}. \tag{15}$$

Then x_R-x_1 is identified with L_{sep} and the constants are expanded to give

$$L_{\mathrm{sep}}\propto\frac{(p_3-p_2)^{3/2}}{\mu_w\rho_w^{1/2}U_0'(0)^2\,\mathrm{Re}_{x_1}}, \tag{16}$$

where $F_0''(0)$ is dropped because it is a constant. With the perfect-gas relation for sound speed,

$$\frac{L_{\mathrm{sep}}}{x_1}\propto\frac{1}{\gamma_1^{3/2}M_1^3}\left(\frac{u_e}{x_1U_0'(0)}\right)^2\left(\frac{\rho_e}{\rho_w}\right)^{1/2}\left(\frac{\mu_e}{\mu_w}\right)\left(\frac{p_3-p_2}{p_1}\right)^{3/2}. \tag{17}$$

Equation (17) is a general result valid for any form of the undisturbed boundary-layer profile. It is important to note the inverse-square dependence on $U_0'(0)$, i.e., the development of shear stress along the dividing streamline is characterized by the wall shear of the incoming boundary layer. Comparisons between computed and predicted wall shear (similar to those for heat flux in Fig. 7) showed that the flat-plate compressible Blasius solution for a laminar boundary layer, with reference-temperature modification, gives a reasonable approximation for skin friction under the present conditions. Evaluating $U_0'(0)$ from Eq. (3) and the definition of C_f gives

$$U_0'(0)=0.332\frac{u_e\mu^*\rho^*}{x_1\mu_w\rho_w}\sqrt{\frac{1}{C^*}}. \tag{18}$$

Substituting this into Eq. (17) results in

$$\frac{L_{\mathrm{sep}}}{x_1}\propto\frac{\Lambda_1}{\gamma_1^{3/2}M_1^3}\left(\frac{p_3-p_2}{p_1}\right)^{3/2}, \tag{19}$$

where

$$\Lambda=\left(\frac{\mu_w}{\mu^*}\right)\left(\frac{T^*}{T_e}\right)\left(\frac{T_w}{T_e}\right)^{1/2}. \tag{20}$$

The dependence on M_1 is identical to that in Eqs. (8) and (9), but the dependence on p_3 does not correspond to previous empirical results. The factor Λ is unique to the present work and describes the effect on skin friction of wall-to-edge temperature ratio for arbitrary viscosity law, the latter accounted for using the reference-temperature concept. For an ideal fluid with $C=1$, Λ reduces to $(T_w/T_e)^{3/2}$. Equation (19) can also be obtained, following Burggraf,[103] by application of the incompressible Bernoulli equation to the asymptotic solution along ψ^*. This is because, within the triple-deck framework, ψ^* resides in a thin incompressible layer.

Equation (19) provides no predictive capability, only a partial scaling for L_{sep}. It is based on the leading-order term of an asymptotic theory for large Re_{x_1}, and therefore cannot predict the functional dependence on Re_{x_1}. In Sec. VI, the new factor Λ is shown to provide some measure of collapse for data spanning a large range in Λ.

V. ANALYSIS OF REAL-GAS EFFECTS

Investigation of mechanisms for real-gas effects on L_{sep} benefits from a broad classification into mechanisms due to processes occurring external and internal to viscous regions of the flow. Within this framework, external real-gas effects are defined as changes in L_{sep} due to chemistry in the external inviscid flow, with respect to a frozen flow with the same free stream, and the effect this has on a nonreacting boundary layer, shear layer, and separation bubble. Internal real-gas effects are defined as changes in L_{sep} due to chemistry in viscous regions of the flow, with respect to a nonreacting boundary layer, shear layer, and separation bubble having the same external inviscid flow conditions. It is important to note the distinction between reference flows. External and internal mechanisms were investigated separately using different techniques.

A. External mechanisms

External mechanisms were investigated using the ideal dissociating gas (IDG) model of Lighthill[109] to estimate local external flow conditions for both equilibrium and frozen flow, and evaluating the relative change in L_{sep}/x_1 between these two flows according to the following empirical perfect-gas scaling law based on local external flow conditions:

$$\frac{L_{\mathrm{sep}}}{x_1} \propto \frac{\Lambda_1 \sqrt{\mathrm{Re}_{x_1}}}{\gamma_1^{3/2} M_1^3} \left(\frac{p_3 - p_2}{p_1} \right), \tag{21}$$

assembled from the Λ, γ, and M_1 behavior of Eq. (19), the Re_{x_1} behavior of Eq. (8), and a linear p_3 behavior consistent with both Eq. (9) and the present experimental results (see Sec. VI A). This method elucidates external mechanisms independently of internal mechanisms. The simplicity of the IDG model permitted efficient investigation of a large parameter space.

1. IDG oblique shocks

The IDG model has previously been applied to oblique shocks by Sanderson.[38] A nondimensional form of the shock jump equations is obtained by introducing the following parameters[110] (written for nitrogen): the static-to-dynamic pressure ratio

$$P = \frac{p}{\rho u^2} \propto \frac{1}{M^2}, \tag{22}$$

the ratio of kinetic energy to dissociation energy

$$K = \frac{u^2}{2 R_{\mathrm{N}_2} \theta_d}, \tag{23}$$

and the ratio of stagnation enthalpy to dissociation energy

$$H_0 = \frac{h_0}{R_{\mathrm{N}_2} \theta_d} = K \left[1 + 2P \left(\frac{4+\alpha}{1+\alpha} \right) \right] + \alpha, \tag{24}$$

where R_{N_2} is the gas constant of N_2, $\theta_d = 113\,200\,\mathrm{K}$ is the characteristic temperature for dissociation of N_2, and α is the atomic mass fraction. For an oblique shock of angle β relative to the upstream flow direction, with upstream and downstream states denoted 1 and 2, respectively, the shock-normal components of P and K are

$$P_{1n} = \frac{P_1}{\sin^2 \beta}, \quad K_{1n} = K_1 \sin^2 \beta. \tag{25}$$

Substituting Eq. (25) in Eq. (24) gives $H_{0_{1n}}$. Using the ideal-gas thermal equation of state

$$p = \rho(1+\alpha) R_{\mathrm{N}_2} T \tag{26}$$

with the IDG caloric equation of state

$$h = R_{\mathrm{N}_2} [(4+\alpha) T + \alpha \theta_d], \tag{27}$$

and introducing the notation $\hat{\rho} = \rho_2/\rho_1$, etc., the conservation equations for momentum and energy can be reduced to a single quadratic equation for the density ratio across an oblique shock,

$$(H_{0_{1n}} - \alpha_2)\hat{\rho}^2 - 2K_{1n}(1+P_{1n}) \left(\frac{4+\alpha_2}{1+\alpha_2} \right) \hat{\rho} + K_{1n} \left(\frac{7+\alpha_2}{1+\alpha_2} \right) = 0. \tag{28}$$

Only one solution corresponds to a shock discontinuity (the other represents relaxation from a nonequilibrium upstream state), given always by the largest root,

$$\hat{\rho} = \frac{K_{1n}(1+P_{1n})(4+\alpha_2)(1+\sqrt{D})}{(H_{0_{1n}} - \alpha_2)(1+\alpha_2)}, \tag{29}$$

$$D = 1 - \frac{(H_{0_{1n}} - \alpha_2)(7+\alpha_2)(1+\alpha_2)}{K_{1n}(4+\alpha_2)^2(1+P_{1n})^2}. \tag{30}$$

Written this way, it is clear a real solution must have

$$H_{0_{1n}} > \alpha_2 \geqslant \alpha_{\min} = fn(\alpha_1, K_{1n}, P_{1n}), \tag{31}$$

where the determinant $D=0$ at $\alpha_2 = \alpha_{\min}$.

For frozen flow, $\alpha_2 = \alpha_1$ and Eq. (29) reduces to

$$\hat{\rho}_{\mathrm{fr}} = \frac{7+\alpha_1}{1+\alpha_1+2P_{1n}(4+\alpha_1)}. \tag{32}$$

For equilibrium flow, an additional equation is required; the IDG equilibrium law of mass action,

$$\frac{\alpha_2^2}{1-\alpha_2} = \frac{\rho_d}{\rho_1} \exp\left\{ \frac{(1+\alpha_2)\hat{\rho}^2}{2K_{1n}[1-\hat{\rho}(1+P_{1n})]} \right\}. \tag{33}$$

The heart of the IDG model is the approximation embodied in Eq. (33), whereby the contribution of internal energy modes to the law of mass action is a weak function of temperature over a wide range and is taken to be constant at an average value ρ_d ($1.3\times10^5\,\mathrm{kg/m^3}$ for N_2). This approximation effectively forces the vibrational energy of the molecular component of the gas to be constant at half of its fully excited value [see Eq. (27)], which is what in practice most limits the usefulness of the model.

Because the flow deflection angle θ is known, and not the shock angle β, another equation is needed to close the problem. From geometrical considerations and conservation of mass,

$$\tan(\beta - \theta) = \frac{\tan \beta}{\hat{\rho}}. \tag{34}$$

Given a wedge angle θ and upstream state (α_1, P_1, K_1, and ρ_d/ρ_1), a steady weak oblique shock solution for $\hat{\rho}$, β, and α_2 was found by simultaneously solving Eqs. (29), (30), (33), and (34) for equilibrium flow, or Eqs. (32) and (34) for frozen flow. Other parameters such as $\hat{u}$, $\hat{T}$, and M_2 were then evaluated explicitly. Sound speed was calculated after Vincenti and Kruger.[111] Viscosity was estimated as in Sec. III C 3.

2. IDG results for separation length

The IDG model for oblique shocks was applied to the inviscid double-wedge configuration shown in Fig. 9. Although this simplified geometry neglects effects due to splitting of the corner shock into two weaker shocks at separation

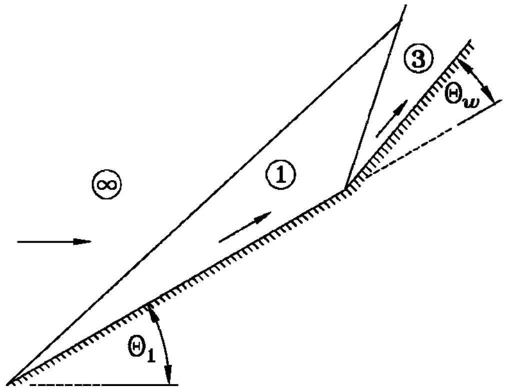

FIG. 9. Notation for IDG double-wedge calculations.

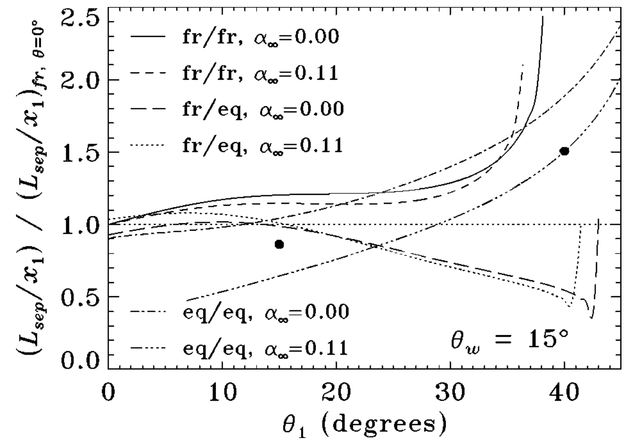

FIG. 11. IDG results for the ratio of $L_{\rm sep}$ to frozen flat-plate solution, plotted against θ_1 with $\theta_w = 15°$ and K_∞, P_∞, and ρ_d/ρ_∞ fixed according to condition C2 at $A_e/A_* = 100$. Three sets of solutions are given: frozen flow on both wedges (fr/fr), frozen flow on first wedge with equilibrium flow on second wedge (fr/eq), and equilibrium flow on both wedges (eq/eq). Each solution set has two values of α_∞ as indicated. Equilibrium curve for $\alpha_\infty = 0.11$ has a minimum in θ_1 at the CJ condition. Frozen curves have a maximum in θ_1 at the detachment condition. (●) The nonequilibrium inviscid triple-wedge computational results for condition C2 with $A_e/A_* = 100$ and $\theta_w = 15°$.

and reattachment, it was necessary because the separation geometry could not be predicted and in any case depends on internal mechanisms. Thus results in Figs. 10 and 11 are presented in terms of $L_{\rm sep}/x_1$, which overemphasizes the effect of external mechanisms on $L_{\rm sep}$ alone. In Eq. (21), p_2 was set equal to $p_{\rm inc}$ found from triple-deck theory,[104,105]

$$\frac{p_{\rm inc}-p_1}{p_1} \sim 1.04\gamma_1 M_1^2 \left(\frac{C^*/{\rm Re}_{x_1}}{M_1^2-1} \right)^{1/4}. \tag{35}$$

Three different solutions were obtained for each geometry and (uniform) free-stream condition specified; one with frozen flow on both wedges, one with equilibrium flow on both wedges, and one with frozen flow on the first wedge and equilibrium flow on the second wedge. The latter solution approximates a case that may arise at lower incidence, where the first shock does not induce a significant reaction rate, but increases the density and temperature enough to cause reactions behind the second shock.

In Fig. 10 are presented IDG results, as the ratio of equilibrium-flow to frozen-flow solutions for $L_{\rm sep}$ according to Eq. (21), for a double-wedge geometry of $\theta_1 = 30°$ and $\theta_w = 15°$ over a large range in H_{0_∞} obtained by varying K_∞ while keeping P_∞ and ρ_d/ρ_∞ fixed. Two sets of values were used for the latter parameters, based on experimental condition C2 with $A_e/A_* = 100$ and 400 as shown in Table II. Though these two cases are denoted in Fig. 10 by the corresponding value of A_e/A_*, the relationship to A_e/A_* holds only for a particular value of K_∞; in a real shock tunnel flow, K_∞ cannot be varied independently of P_∞ without also changing A_e/A_*. The classification by A_e/A_* is intended to represent the highest and lowest free-stream density attainable in the high-enthalpy experiments. Two cases were also considered for the free-stream dissociation; the partially dissociated condition ($\alpha_\infty = 0.11$) produced by T5, and a non-dissociated condition ($\alpha_\infty = 0$) corresponding to free flight at the same P_∞, K_∞, and ρ_d/ρ_∞ as the experiment. The curves for $\alpha_\infty = 0.11$ in Fig. 10 terminate [outside the plot range in

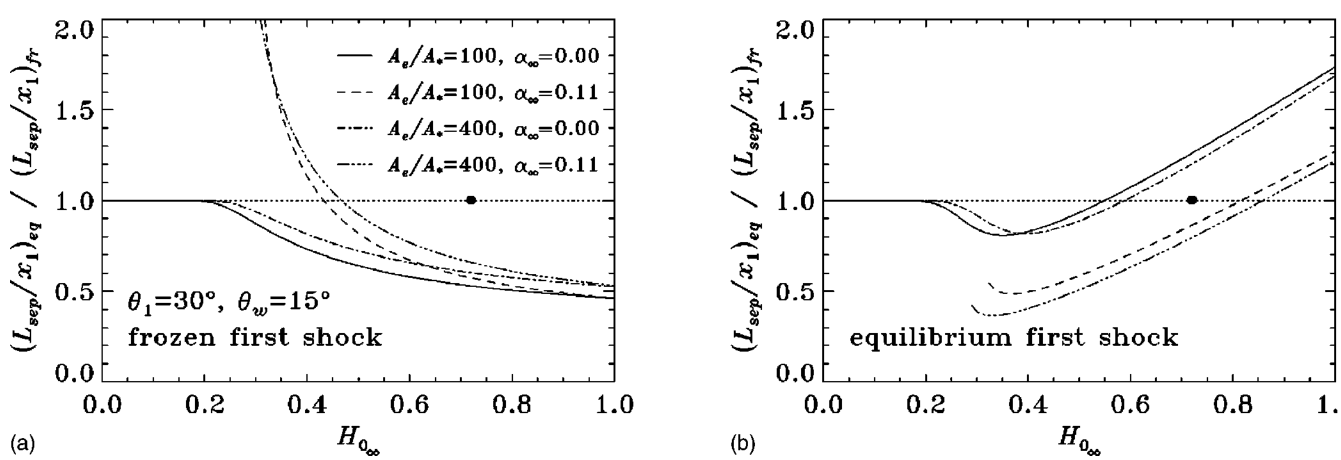

FIG. 10. IDG results for $L_{\rm sep}$ plotted against H_{0_∞} with $\theta_1 = 30°$ and $\theta_w = 15°$, with P_∞ and ρ_d/ρ_∞ fixed according to condition C2 at $A_e/A_* = 100$ and 400, and with α_∞ varied independently as indicated; (a) equilibrium-to-frozen ratio of $L_{\rm sep}$ with frozen flow on first wedge; (b) equilibrium-to-frozen ratio of $L_{\rm sep}$ with equilibrium flow on first wedge. Curves for $\alpha_\infty = 0.11$ exhibit a minimum in H_{0_∞} at the CJ condition. (●) The nonequilibrium inviscid double-wedge computational result for condition C2 with $A_e/A_* = 225$, $\theta_1 = 30°$, and $\theta_w = 15°$.

TABLE II. Approximate values of the nondimensional free-stream parameters for condition C2 at two values of A_e/A_*.

A_e/A_*	P_∞	K_∞	H_{0_∞}	ρ_d/ρ_∞	α_∞
100	0.034	0.48	0.71	1.2×10^7	0.11
400	0.017	0.51	0.70	3.2×10^7	0.11

Fig. 10(a)] on recombination branches at a minimum θ_1 corresponding to the Chapman–Jouget limit for exothermic discontinuities.

With frozen flow on the first wedge, the only difference between frozen and equilibrium solutions arises in region 3, thus the result in Fig. 10(a) is due entirely to changes in p_3. Dissociation in region 3 causes a lower pressure and hence a reduction in L_{sep}, by as much as 50% at $H_{0_\infty}=1$. On recombination-solution branches, p_3 and L_{sep} increase drastically, but equilibrium recombination shocks are generally not found in shock tunnel flows where recombination rates are low. With equilibrium flow on the first wedge, Re_{x_1}, M_1, and Λ_1 all increase with dissociation, while p_3/p_1 may increase or decrease depending on α_∞ and H_{0_∞}; the result in Fig. 10(b) similarly depends on α_∞ and H_{0_∞}. The increase in M_1 dominates at moderate enthalpy, and an increase in both Λ_1 and p_3/p_1 dominates at high enthalpy.

To gauge the importance of these effects under typical experimental conditions, one case was recomputed using the full thermochemical nonequilibrium code (see Sec. III) instead of the IDG model, with the free stream initialized according to an experiment with $A_e/A_*=225$. The result is represented by a single point in Fig. 10. Only a slight departure from frozen-flow conditions was found in region 1, the effects on Re_{x_1}, M_1, and Λ_1 canceling each other in the scaling for L_{sep}. The combined nonequilibrium effects in regions 1 and 3 result in negligible change in p_3/p_1. External mechanisms are not important at this condition.

Results from a second study for fixed stagnation enthalpy and varying incidence angle $0°<\theta_1<45°$, with flap deflection angle fixed at $\theta_w=15°$, are presented in Fig. 11. Frozen–frozen, frozen–equilibrium, and equilibrium–equilibrium solutions are shown independently, each normalized by the flat-plate ($\theta_1=0°$) frozen-flow solution. Two values of α_∞ are again considered, but only $A_e/A_*=100$. The variation of L_{sep} with θ_1 for frozen–frozen and frozen–equilibrium solutions is generally nonmonotonic due to competition between decreasing Λ_1 and p_3/p_1 on the one hand, and increasing Re_{x_1} plus decreasing M_1 on the other hand. For the equilibrium–equilibrium solutions, L_{sep} increases continuously with θ_1, passing the flat-plate frozen-flow value at an intermediate incidence angle. At high incidence, only the frozen–equilibrium solutions differ greatly from the frozen–frozen solutions. Two cases were recomputed using the nonequilibrium code, but due to inconsistencies with the IDG model (free-stream nonuniformity, vibrational modeling, etc.), care must be taken interpreting the results. Slight nonequilibrium recombination was found at $\theta_1=15°$, which may explain why this result lies between frozen and equilibrium solutions. At $\theta_1=40°$, strong nonequilibrium dissociation occurs throughout the flow, and the result appears close to the equilibrium–equilibrium IDG solution.

3. Relation to previous results

A decrease in L_{sep} compared to frozen flow was observed for equilibrium compression-corner flows ($\theta_1=0°$) analyzed by Anders and Edwards[21] and computed by Grasso and Leone,[17] as well as for nonequilibrium shock-impingement flow computed by Furumoto *et al.*[45] In each of these cases, there is no dissociation upstream of separation, so the only external mechanism available is the effect of dissociation on reattachment pressure. Internal mechanisms are not necessarily negligible, but they either act in the same direction or are weaker than the external mechanism. The decrease in L_{sep} found by Brenner *et al.*[42] and by Oswald *et al.*[43] for equilibrium hyperboloid-flare flow, with nondissociated free stream, is not so easily explained by external mechanisms. Though an axisymmetric configuration, the hyperboloid flare has flow-deflection angles similar to the geometry in Fig. 10. The free-flight condition used by Brenner *et al.*[42] has a free-stream density two orders of magnitude lower than found in T5. The equilibrium IDG solutions in Fig. 10(b) show that as A_e/A_* increases (i.e., as ρ_∞ decreases), the value of H_{0_∞} at which $(L_{\mathrm{sep}})_{\mathrm{eq}}=(L_{\mathrm{sep}})_{\mathrm{fr}}$ increases. This could explain by external mechanisms the decrease in L_{sep} for equilibrium hyperboloid-flare flows at low-density free-stream conditions, if in fact external mechanisms dominate these flows. Similar reasoning may explain the decrease in L_{sep} observed experimentally by Krek *et al.*[40] for hyperboloid-flare flows. The shock-impingement flows studied by Ballaro and Anderson[47] and by Grumet *et al.*[48] are analogous to the case of a compression corner with $\theta_1=0°$ and $\alpha_\infty>0$. Their results are not consistent with external mechanisms, except perhaps the high-pressure case computed by Grumet *et al.*[48] with recombination downstream of reattachment, which could increase p_3 and contribute to the observed increase in L_{sep}. Internal mechanisms are probably important in these flows.

The present experimental measurements of physical separation length could not be used to verify external mechanisms, for the following reasons: (1) external mechanisms could not be separated from unknown internal mechanisms which also existed in the experiments; (2) low-enthalpy frozen and high-enthalpy reacting flows in the experiments had different free-stream conditions and could not be directly compared with each other as done in the IDG study; (3) the free-stream conditions in high-incidence experiments often did not admit a frozen-flow solution (due to shock detachment). The IDG results indicate that external mechanisms were only important in the experiments with high incidence, and depend on free-stream dissociation which does not exist for free flight.

B. Internal mechanisms

Mechanisms for real-gas effects occurring internal to viscous regions of the flow may be further subdivided into those arising upstream or downstream of separation. Considering the scaling in Eq. (17), the upstream boundary layer

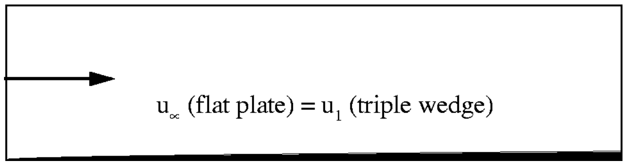

FIG. 12. Sketch of domain for nonequilibrium boundary-layer computations showing initialization.

affects L_{sep} through changes in the undisturbed wall shear stress; this was studied using the nonequilibrium code described in Sec. III under conditions derived from the experiments. Thermochemical nonequilibrium processes in the shear layer and separated region must also affect L_{sep}, but these cannot be included in a scaling based on Eq. (17), and are only briefly considered.

1. Computational boundary-layer study

A limited number of flat-plate boundary-layer computations were performed with uniform free-stream conditions based on inviscid triple-wedge computational results just upstream of separation, as indicated in Fig. 12. The grids contained 100×75 cells, clustered at the leading edge with a minimum spacing of 50 μm, and at the wall with 35 cells inside the displacement thickness estimated from frozen-flow theory. Boundary-layer profiles were extracted 5 cm from the leading edge, half the 10 cm grid length. Further grid refinement at the leading edge changed the solution at $x=5$ cm by less than 0.5%. Excellent grid resolution in the transverse direction is shown on some of the profiles in Figs. 13 and 16 by points corresponding to cell centers. Eight cases computed are described in Table III. For cases 1 and 2, the nonequilibrium flow state taken from the triple-wedge result was significantly departed from a frozen or equilibrium flow state, such that α_e increased with x and produced a nonnegligible difference between edge conditions of reacting and frozen solutions at $x=5$ cm. To permit a direct comparison, the free-stream initialization of each frozen-flow computation was modified to match the external flow at $x=5$ cm in the corresponding nonequilibrium computation; the modified conditions are shown separately in Table III.

For all low-enthalpy cases, nonequilibrium computations indicated a chemically frozen boundary layer. Profiles of α for the high-enthalpy cases are shown in Fig. 13. The boundary-layer thickness δ was taken as the location of the first grid point for which $u>0.99u_e$. For the noncatalytic results, α_w decreased with distance from the leading edge, the value at $x=5$ cm depending on the recombination rate. Though not evident on the scale used in Fig. 13, the noncatalytic curves do exhibit $\partial\alpha/\partial y=0$ at the wall.

2. Upstream boundary layer

The effect of boundary-layer recombination on the wall shear stress is presented in Fig. 14 as the ratio of reacting to frozen C_f plotted against a simple gas-phase Damköhler number, similar to one given by Rae,[112]

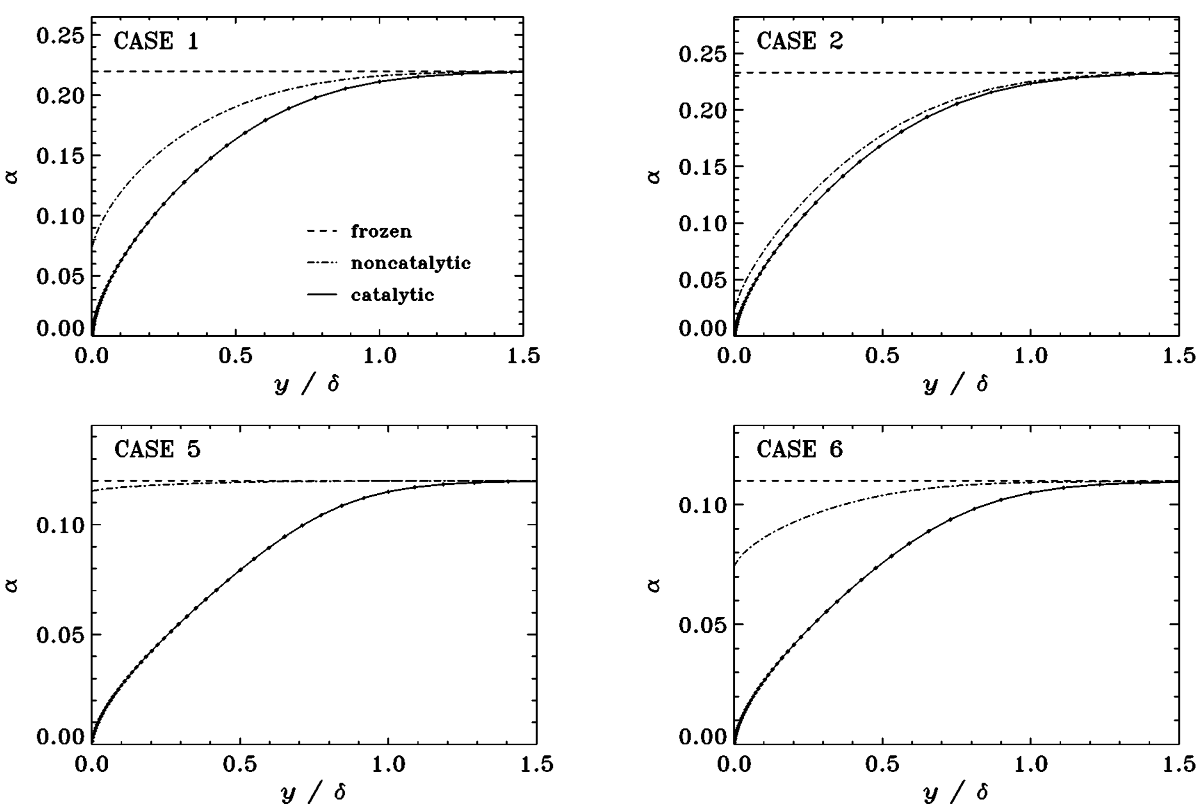

FIG. 13. Selected computational boundary-layer results for α; frozen flow (---), nonequilibrium flow with noncatalytic wall (-··-), and nonequilibrium flow with catalytic wall (—). Points on catalytic-wall curves indicate cell centers from computational grid. The cases are described in Table III.

TABLE III. Description of cases encompassed by the computational boundary-layer study. Designations F, N, and C refer to frozen flow, nonequilibrium flow with noncatalytic wall, and nonequilibrium flow with catalytic wall, respectively. The last three columns give experimental conditions on which free-stream properties are based.

Case no.	ρ_∞ (kg/m^3)	u_∞ (m/s)	T_∞ (K)	T_{u_∞} (K)	α_∞	M_∞	Re_∞ $L=5$ cm	T5 cond.	A_e/A_*	θ_1
1N/C	0.015	3000	7200	7400	0.21	1.61	1.24×10^4	C2	400	40°
1F	0.015 06	3023	6921	6967	0.2198	1.65	1.30×10^4			
2N/C	0.055	2900	6700	6700	0.23	1.60	4.65×10^4	C2	100	40°
2F	0.055 24	2906	6600	6603	0.2333	1.61	4.73×10^4			
3	0.015	1700	3600	3300	0.0002	1.45	1.28×10^4	B1	400	40°
4	0.025	1700	3600	3300	0.0005	1.45	2.14×10^4	B1	225	40°
5	0.008	5600	3000	4200	0.12	4.88	2.50×10^4	C2	400	15°
6	0.022	5300	4400	4300	0.11	3.84	4.88×10^4	C2	100	15°
7	0.009	3300	940	3300	0.0005	5.49	3.94×10^4	B1	400	15°
8	0.015	3200	1000	3100	0.0005	5.16	6.10×10^4	B1	225	15°

$$\Gamma = \frac{x}{u_e}\left(\frac{d\alpha}{dt}\right)_{w,\alpha=\alpha_e}, \tag{36}$$

where $d\alpha/dt$ is evaluated at the wall temperature and density but the free-stream composition, and x/u_e characterizes the streamwise flow time. Skin friction increases with recombination, but only a small amount (less than 5% over the cases studied). For a catalytic wall, the increase depends only on α_e; since equilibrium is enforced at the wall, the parameter Γ has no importance. For a noncatalytic wall, the increase occurs gradually with increasing $-\Gamma>100$ as α_w decreases. The discrepancy for cases 3 and 4 arises probably from vibrational nonequilibrium in the free-stream initialization, causing mismatched edge conditions between frozen and reacting solutions similar to that already alleviated in cases 1 and 2. According to Eq. (17), the increase in C_f observed here may induce a small decrease in L_{sep} with respect to a frozen boundary layer with the same partially dissociated edge conditions.

The present result is not consistent with a previous suggestion by Mallinson *et al.*[36,37] that L_{sep} should increase for a recombination-dominated boundary layer. They considered chemical energy released or absorbed along a streamline, and the effect this has on temperature and density profiles which determine boundary-layer thickness. The difference between frozen and equilibrium flows was considered as an exchange between chemical and thermal energy at constant pressure, enthalpy, and specific heat capacity; thus recombination increases temperature, decreases density, and increases δ. The relationship between δ and C_f appears straightforward; at constant Re_x, increasing δ stretches the velocity profile in physical coordinates, resulting in a lower shear stress at the wall. For the present computational study, a slight (<2%) decrease in δ was observed for cases 1 and 2.

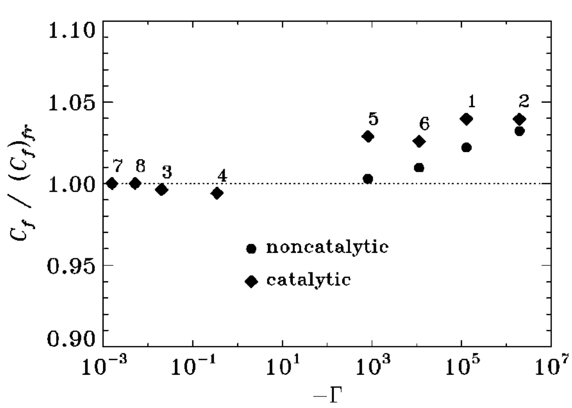

FIG. 14. Comparison between frozen and reacting computational boundary-layer results for C_f, plotted against the nondimensional reaction-rate parameter Γ given by Eq. (36). (◆) Catalytic-wall results, (●) noncatalytic-wall results. Numbered cases are described in Table III.

The present result is, however, consistent with the result of Ikawa,[46] who showed a decrease in L_{sep} and δ due to recombination by applying an extended momentum integral method to the case of fully dissociated edge condition and fully recombined wall condition. He assumed that diffusion dominates over recombination, which taken together with the result of Mallinson *et al.*,[37] might suggest that diffusion and recombination have compensating effects on C_f. In fact, careful examination of the present computational results showed that the phenomenon is more complicated than implied by either of these approximate methods.[55]

Temperature profiles are shown in Fig. 15 for two cases. Though temperature generally increases with recombination [Fig. 15(a)], it can also decrease with recombination as seen for the outer part of the boundary layer in Fig. 15(b). The effect of boundary-layer recombination cannot be described by a simple exchange between chemical and thermal energy; energy released by recombination may be carried away by conduction or diffusion. The temperature decrease in Fig. 15(b) coincides with regions where $\partial T/\partial y<0$ or $\partial^2 T/\partial y^2>0$, two conditions which do not exist in Fig. 15(a). It can be shown, by expanding conduction and diffusion terms found in any differential form of the energy conservation equation for reacting flow, that the sign and magnitude of various enthalpy and mass-fraction derivatives are important in determining the effect of recombination on temperature. Streamwise derivatives can also be important, especially for a noncatalytic wall.

The velocity profile is modified only indirectly by real-gas effects, from changes in the physical scale related to changes in the Chapman–Rubesin parameter C and the density profile. In particular, a generalized compressible

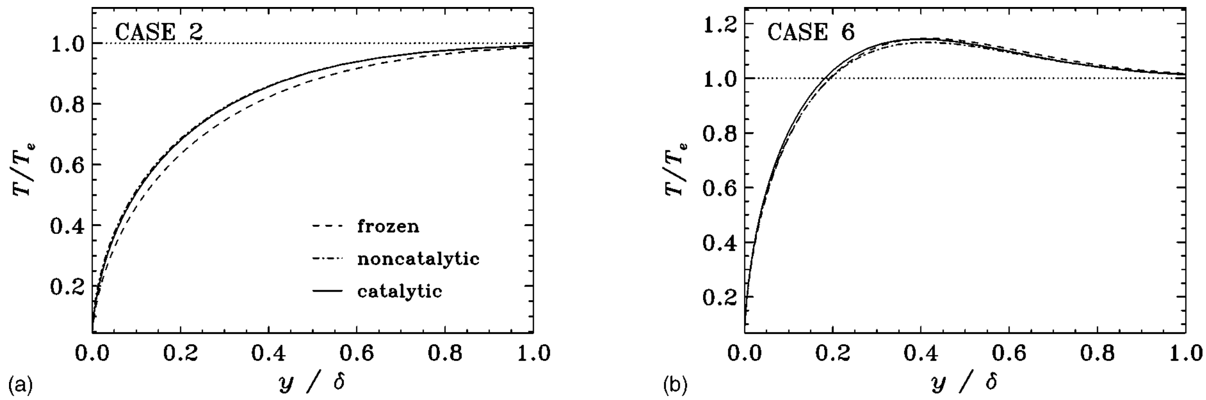

FIG. 15. Selected computational boundary-layer results for T/T_e. Cases are described in Table III.

boundary-layer similarity transformation for the normal coordinate,[113] with C assumed constant and taken into the transformation variable η, can be inverted to give $y \propto \sqrt{C}\int(\rho_e\, d\eta/\rho)$; increasing C stretches the scale and decreases $\partial u/\partial y$ while increasing ρ has the opposite effect. Changes in viscosity, on which both C and C_f depend, follow changes in temperature because μ depends only weakly on α. Changes in density, however, depend on changes in both α and T through the thermal equation of state at constant pressure,

$$\frac{\rho}{\rho_{\mathrm{fr}}} = \frac{T_{\mathrm{fr}}}{T}\left(\frac{1+\alpha_e}{1+\alpha}\right). \tag{37}$$

Thus density may increase or decrease with recombination. An increase in the shear stress τ with recombination was found everywhere in the computations except the outer part of the boundary layer in cases 5 and 6, where the temperature decreased.

To emphasize these ideas, near-wall ($y \leqslant 0.1\delta_{\mathrm{fr}}$) profiles of reacting-to-frozen ratios of three parameters from the solutions for case 2, as well as nondimensional mass-fraction gradient, are presented in Fig. 16 using a log coordinate. The large increase in T for a noncatalytic wall, twice that found for a catalytic wall, coincides with the region where $\partial^2\alpha/\partial y^2$ changes sign, indicating the importance of species gradients

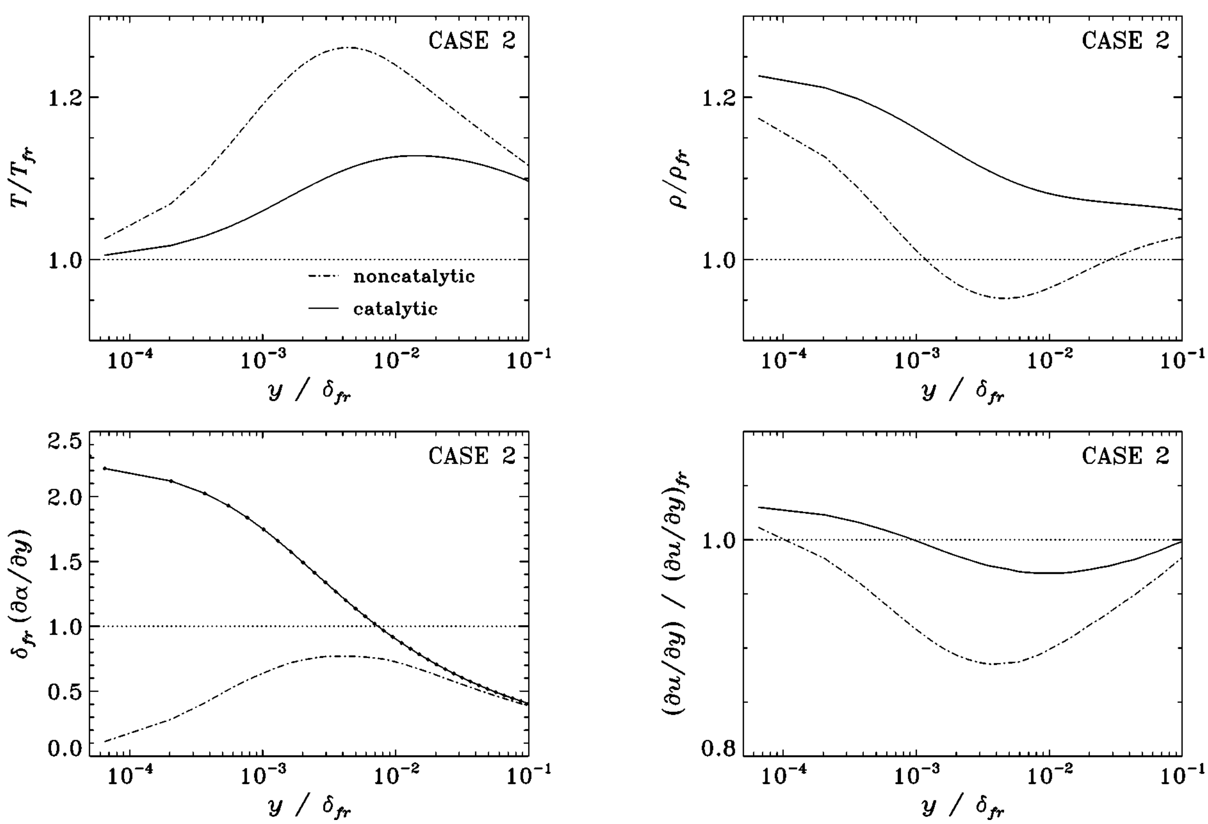

FIG. 16. Near-wall ($y \leqslant 0.1\delta_{\mathrm{fr}}$) boundary-layer profiles of reacting-to-frozen solution ratios for T, ρ, and $\partial u/\partial y$, as well as nondimensional mass-fraction gradient, for computational case 2 described in Table III. Curves terminate at the center of the wall-adjacent computational cell. Points on the catalytic-wall curve for $\delta_{\mathrm{fr}}(\partial\alpha/\partial y)$ indicate cell centers from computational grid.

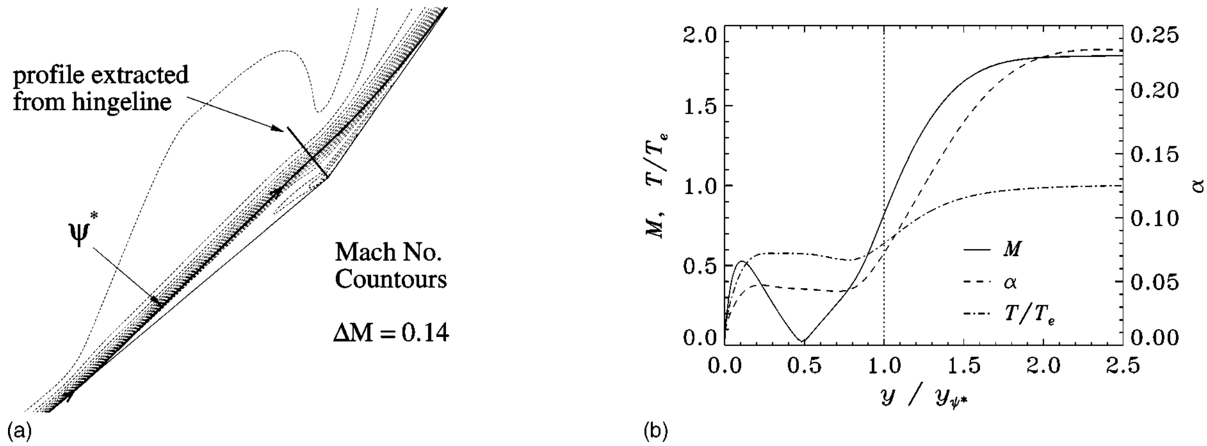

FIG. 17. Viscous double-wedge computational results in the separation region for shot 1796 (condition C2, $A_e/A_* = 100$, $\theta_1 = 40°$, $\theta_w = 15°$); (a) Mach number contours, dividing streamline ψ^*, and line from which shear-layer profile is extracted; (b) profiles of M (—), α (---), and T/T_e (-··-, $T_e = 6940$ K) through the separated shear layer with y nondimensionalized by the distance to ψ^*.

in determining the effect of recombination on temperature. In this same region, the change in T for a noncatalytic wall dominates the change in α in Eq. (37), producing a decrease in ρ with recombination. Very close to the cold wall, the temperature is constrained and ρ increases due to the decrease in α, while the chemical energy released by recombination is conducted to the wall by the large temperature gradient. The effect of recombination on the velocity gradient is dominated at the wall by the increase in ρ, with $(\partial u/\partial y)/(\partial u/\partial y)_{\mathrm{fr}} > 1$ at the wall-adjacent computational cell despite the large value of C/C_{fr} (not shown) and, for a noncatalytic wall, despite the region of decreased density a slight distance away from the wall. Because μ increases with T in the same region that $(\partial u/\partial y)/(\partial u/\partial y)_{\mathrm{fr}} < 1$, the increase in τ (not shown) remains almost constant for $y < 0.1\delta_{\mathrm{fr}}$.

In summary, the increased skin friction seen in Fig. 14 for reacting flow over frozen flow is due entirely to the dilatational effect of increased density at the wall which occurs for recombination under the condition of constrained wall temperature. The authors know of no other published results for recombination-dominated flat-plate boundary layers. Of those works considering dissociation-dominated flat-plate boundary layers,[112,114–118] only the paper by Moore[118] looked at the effect of reactions on skin friction, finding an increase at very high wall enthalpy.

3. Separated shear layer

Qualitative consideration of mechanisms for real-gas effects arising downstream of separation was aided by examination of the viscous double-wedge computational results (see Sec. III C 4); unfortunately, the same configurations did not admit frozen-flow solutions for comparison. Figure 17(a) shows the line through the shear layer from which the profiles in Fig. 17(b) were extracted. Recombination occurs in the shear layer above ψ^*, while α and T remain constant over much of the separation bubble. The dissociation fraction along the wall and along the dividing streamline (approximated here by taking a streamline very close to the wall upstream of separation) are shown in Fig. 18. Upstream of separation, α_w decreases from the free-stream value due to nonequilibrium gas-phase recombination in the boundary layer near the noncatalytic wall. Downstream of separation, α_w drops precipitously, but the partially recombined gas which follows the dividing streamline begins dissociating again as soon as it leaves the wall.

The mass-fraction gradients in Fig. 17(b) are very small over much of the recirculating region, which, as suggested by the near-wall noncatalytic result in Fig. 16, may result in a temperature rise due to recombination high enough to dominate the change in α, giving a lower density and hence a larger separation bubble. The present model for separation length [Eq. (13)], however, considers the shear stress τ along ψ^*, and as discussed in Sec. V B 2, changes in τ due to recombination are not necessarily related directly to the dilatational effect of changes in ρ, but depend as well on changes in μ and C. It should also be noted that the mechanism which increases C_f in a recombining boundary layer was found to arise from an extreme thermal wall condition that does not exist near ψ^* in a shear layer. It can be seen from Fig. 17(b) that $\partial^2\alpha/\partial y^2 > 0$ and $\partial^2 T/\partial y^2 > 0$ near ψ^*, a combination of derivatives which does not occur in the boundary layer. The streamwise derivatives also differ

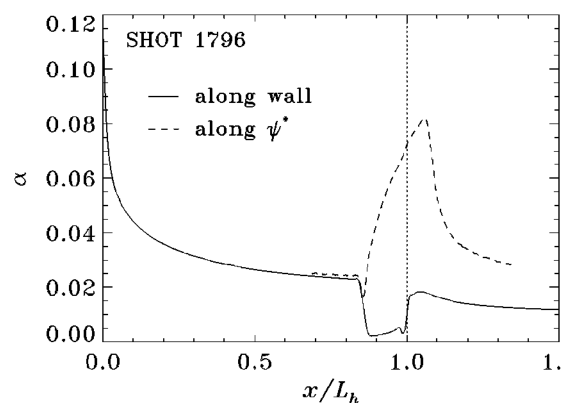

FIG. 18. Viscous double-wedge computational results for α near the wall (—) and along ψ^* (---) for shot 1796 (described in Fig. 17). Distance along the streamline is projected on the wall in a direction perpendicular to the first wedge surface.

greatly between the shear layer and the wall upstream of separation, as shown by Fig. 18. The present computations cannot verify the effect of recombination on $\tau_{\psi*}$, but it is speculated that the present experimental result discussed in Sec. VI (increased L_{sep} from recombination downstream of separation) might result from a decrease in $\tau_{\psi*}$ due to the particular combination of thermal and species gradients found near ψ^*.

The laminar shear layer in compressible flow has been studied by a number of authors,[119–122] but not in the context of a dissociating or recombining gas. One previous result of interest, from a study of base flow by Denison and Baum,[121] is that a hot recirculating region gives significantly larger L_{sep} than a cold recirculating region. Recombination inside the recirculating region may cause the same effect with respect to frozen flow.

4. Relation to previous results

Many previous computational results for shock/boundary-layer interaction in reacting flow show increased skin friction downstream of reattachment compared to frozen flow,[17,45,47,48] regardless of free-stream dissociation, boundary-layer dissociation or recombination, wall catalyticity, and wall temperature (with $T_w \leqslant T_e$). With the present results indicating increased skin friction as well, this suggests that reactions in the boundary layer act to increase the wall shear stress under any situation, except perhaps for a hot wall. The decrease in separation length for reacting flow observed by Furumoto *et al.*[45] and by Grasso and Leone[17] may be partially due to dissociation occurring in the separation region, but the behavior can be explained by external mechanisms. The large increase in L_{sep} observed by Grumet *et al.*[48] for strong recombination in the separation region at high pressure is consistent with the present experimental result (see Sec. VI C). At low pressure, Grumet *et al.*[48] found that L_{sep} was slightly smaller for a catalytic wall than for a noncatalytic wall, consistent with the present computational results showing higher skin friction for a catalytic wall when the reaction rate is not high (see Fig. 14). The case computed by Ballaro and Anderson,[47] also at low pressure, showed a slight decrease in L_{sep} for reacting flow compared to frozen flow (despite some recombination in the separation region).

Recombination might occur in the separated region of the hyperboloid-flare flow studied by Brenner *et al.*,[42] but in this case the frozen reference flow is everywhere undissociated and the decrease in L_{sep} is probably dominated by external mechanisms. It is important to emphasize that the internal real-gas effects presently considered are defined as changes in L_{sep} with respect to frozen flow with the same local external conditions, not with the same free-stream conditions.

VI. EXPERIMENTAL RESULTS

In this section, experimental separation length data, obtained by the methods in Sec. II, are presented with the aid of computational and theoretical results from Secs. III and IV. Interpretation benefits from the framework developed in Sec. V to describe real-gas effects.

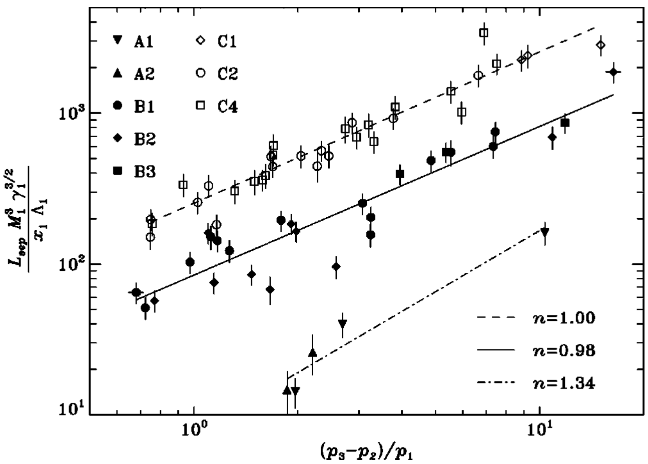

FIG. 19. Experimental L_{sep} data correlated against $(p_3-p_2)/p_1$ from computations. Different symbols represent the different shock tunnel conditions described in Table I, as indicated by the legend. Error bars include measurement uncertainty in L_{sep} and uncertainty in the computed parameters due to uncertainty in reservoir conditions. Lines represent fits to select sets of conditions (-··-A1–2; —B1–3, ---C1–4), and n is the slope of each line in log–log coordinates.

A. Application of new scaling

The theoretical result in Eq. (19) has a dependence on reattachment pressure ratio different from previous results which suggest either a quadratic [Eq. (8)] or linear [Eq. (9)] behavior. For the present experiments, this power-law dependence was found by empirical correlation of L_{sep} scaled by the other parameters in Eq. (19), as shown in Fig. 19. The only parameter measured directly from experiment was L_{sep}/x_1; all other parameters were obtained from the inviscid triple-wedge computations, with viscosities in Λ_1 calculated as in Sec. III C 3. The data do not collapse to a single line, but when they are divided into subsets based on stagnation enthalpy, straight lines fit to each subset in log–log coordinates indicate an average dependence on the pressure ratio factor that is close to linear. The scarcity of data at conditions A1–2 prevents a useful fit in this range, the slope of the line being controlled heavily by a single datum. Replotting Fig. 19 using experimental measurements for p_3 (averaged over selected transducers downstream of reattachment), with p_2 evaluated from Eq. (35), increases the relative scatter of the data but has virtually no effect on the slope obtained from linear fits in log–log coordinates.

A linear dependence on the pressure ratio has previously been found for supersonic interactions[18] and for transitional or turbulent interactions.[102] The present experimental data reside in the supersonic regime with $1<M_1 \lesssim 5$. The apparent difference between supersonic and hypersonic interactions among previous results for pressure ratio dependence [see Eqs. (8) and (9)] might be explained by a change in the reattachment process from an essentially isentropic process in supersonic interactions to a nonisentropic process in hypersonic interactions, for which the reattachment shock forms closer to the wall. In the latter case, a loss in total pressure at reattachment could require a longer separation length to overcome the same rise in static pressure.

The value of Λ_1 is shown in Fig. 20(a) to vary by more

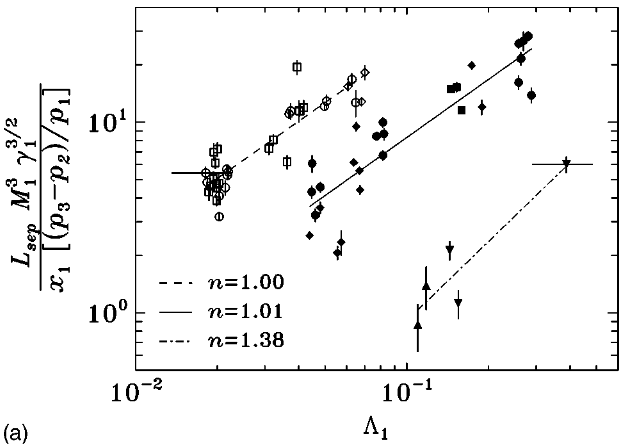

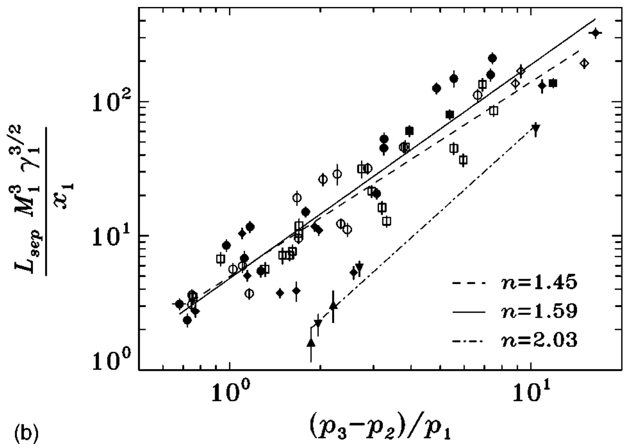

FIG. 20. Effect of Λ_1 on correlation of experimental L_{sep}; (a) correlation of scaled L_{sep} against Λ_1, (b) repeat of the pressure correlation in Fig. 19 with Λ_1 removed from the L_{sep} scaling. Symbols, error bars, lines, and n are described in Fig. 19.

than an order of magnitude over the experimental conditions. There is a tendency for high-enthalpy experiments to have low Λ_1 and low-enthalpy experiments to have high Λ_1, with some overlap. Thus it is not surprising to see that when Λ_1 is removed from the L_{sep} scaling as shown in Fig. 20(b), the high-enthalpy and low-enthalpy data which were segregated in Fig. 19 now fall in the same region. The scatter in Fig. 19 is larger than the error bars, which include measurement uncertainty in L_{sep} and the reservoir conditions but none of the other uncertainties due to approximations involved in the computations, assumptions used to write Eq. (13), or the derivation of Λ_1 from flat-plate boundary-layer theory using the reference temperature. If Λ_1 is removed from the scaling, however, the relative scatter becomes noticeably worse.

The apparent increase in relative scatter for each subset of data when Λ_1 is removed from the scaling was quantified using statistical analysis of the relative root-square deviations,

$$d=\sqrt{\left(\frac{\mathscr{L}-\mathscr{L}_{\mathrm{fit}}}{\mathscr{L}_{\mathrm{fit}}}\right)^2}, \tag{38}$$

where $\mathscr{L}$ are data for the ordinate of scaled L_{sep} in Fig. 19 or 20(b), and $\mathscr{L}_{\mathrm{fit}}$ are values for the ordinate predicted by the curve fits. In Table IV are given the mean $\bar{d}$ and standard deviation σ for each set of relative deviations; low-enthalpy and high-enthalpy conditions, with and without inclusion of Λ_1 in the scaling. The mean deviation from each curve fit is clearly smaller when Λ_1 is included in the scaling. The statistical significance of the difference in $\bar{d}$ was determined by a statistical test of the null hypothesis that both sets of deviations have the same population mean. The appropriate test statistic for unknown population standard deviations and unequal sample standard deviations relies on Student's two-sided t-distribution.[123] As shown in Table IV, the confidence that the reduction in scatter (when Λ_1 is employed) is statistically significant is approximately 92% for the low-enthalpy data and >99% for the high-enthalpy data.

TABLE IV. Statistical analysis of scatter in L_{sep} correlations; the scatter is quantified by the mean $\bar{d}$ and standard deviation σ of the relative deviations d defined by Eq. (38), and P is the two-sided probability, based on a test statistic using Student's t-distribution, that the increase in $\bar{d}$ when Λ_1 is removed has no statistical significance.

	With Λ_1		Without Λ_1		
Condition	$\bar{d}$	σ	$\bar{d}$	σ	P
B1–3	0.293	0.288	0.533	0.631	0.081
C1–4	0.157	0.155	0.318	0.248	0.002

It has been shown qualitatively by numerous previous investigations in perfect-gas flows that L_{sep} increases with increasing T_w/T_1 (see Sec. I A 1), and Λ_1 quantifies this effect by linking T_w/T_1 to the skin friction of the incoming boundary layer using the reference-temperature method and the scaling from triple-deck theory. The resulting dependence on T_w/T_1 is consistent with previous qualitative results. In addition, the large range in T_w/T_1 suggests that any dependence of L_{sep} on T_w/T_1 is important in the present experiments. The use of Λ_1 also recovers the linear dependence on pressure ratio found in previous results for supersonic interactions. Thus the new factor Λ_1 introduced in the present work accounts at least approximately for wall temperature effects on separation length. The fact that it also segregates the high-enthalpy and low-enthalpy data from each other is attributed in Sec. VI C to real-gas effects. The factor $\gamma^{3/2}$ varies only a small amount in the present experiments.

B. Reynolds-number effects

Separation length scaled by all the other parameters, using the linear pressure ratio dependence found for the present experiments, is plotted against Re_{x_1} in Fig. 21. This plot appears similar to one presented by Needham and Stollery,[27,53] which correlates several authors' results against Re_{x_1} and shows a precipitous drop in scaled separation length due to transition occurring upstream of reattachment. The sharp decrease in Fig. 21 occurs over a range of Re_{x_1} $(1-4\times10^5)$ significantly lower than that found by Needham and Stollery $(1-4\times10^6)$. The present data, however, exhibit the same

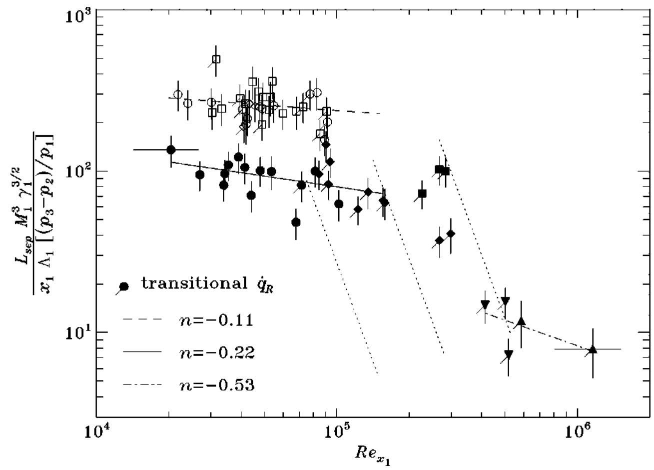

FIG. 21. Correlation of experimental L_{sep} against Re_{x_1} from computations. Symbols, error bars, line fits, and n are described in Fig. 19. Flagged symbols indicated suspected transitional interactions, which are excluded from the fits for conditions B1–3 and C1–4. Dotted lines are a visual aid to show possible transitional paths.

behavior in that transition occurs for smaller Re_{x_1} as θ_w is increased while the conditions in region 1 are kept constant. This result is explained simply by the increase in L_{sep} with increasing θ_w; the location of transition in a free-shear layer depends on distance from its origin at separation. In addition, transitional or turbulent structures in the boundary layer downstream of reattachment were evident in some of the corresponding interferograms.

The most reliable indicator of transition was comparison of measured heat flux in the reattachment region to predictions based on laminar and turbulent models as described in Sec. III C 4. The predictions were computed for every shot in Fig. 21, including additional predictions for high-enthalpy experiments using the $\alpha_w=0$ approximation, and additional predictions for all shots based on edge conditions corrected using experimental pressure measurements. Any shot with heat flux measurements falling above the laminar predictions by more than about 25% of the difference between laminar and turbulent predictions was assumed to be transitional, and the corresponding data in Fig. 21 are flagged as indicated. In making the determination, consideration was given to the accuracy of predictions upstream of separation, the availability of pressure-corrected predictions, and the possibility of obscurement by the effects of strong shock–shock interaction. Based on the results of this comparison, it is clear that experiments at moderate to high Reynolds number suffered transition upstream of reattachment, causing the observed drop in separation length.

The large difference in transition Reynolds number between the present results and those of Needham and Stollery[27,53] is likely due to the destabilizing effects of lower Mach number[95,124–126] and lower wall temperature[124] in the present experiments. For shear-layer transition, the Reynolds number of importance is based on distance from the origin of the shear layer, denoted here as $\mathrm{Re}_{L_{\mathrm{sep}}}$ and evaluated for the present experiments using L_{sep} measurements and inviscid triple-wedge computational results in region 2. Transition is shown to occur for a number of shots in the range $2\times10^4<\mathrm{Re}_{L_{\mathrm{sep}}}<2\times10^5$, corresponding to $2<M_2<5$. Compilations of data by Birch and Keyes[126] and by King *et al.*[125] both indicate transition Reynolds number on the order of 10^5 but varying by at least a factor of 4 over this range in Mach number. Larson and Keating[124] showed also that the transition Reynolds number can decrease well below 10^5 with decreasing T_w/T_{aw}. Even low-enthalpy conditions in the present experiments have T_w/T_{aw} an order of magnitude lower than they investigated. This effect may also explain the earlier transition seen in Fig. 21 for high-enthalpy conditions. The unknown acoustic disturbance levels are probably not a factor; the experiments of King *et al.*[125] with laminar and turbulent nozzle wall boundary layers showed virtually no effect of the noise environment on transition of a separated shear layer.

The present results in Fig. 21 do not show a square-root dependence on Re_{x_1} for laminar interactions as found by Needham,[12] but the present data also cover a limited range in Re_{x_1} and have a high degree of scatter, thus making it very difficult to obtain an empirical correlation with Re_{x_1} to any reasonable accuracy. An important observation from Fig. 21 is that the dependence on Re_{x_1} is not significantly different between high-enthalpy and low-enthalpy experiments with laminar interactions, i.e., a Reynolds-number effect cannot account for the shift in high-enthalpy data above low-enthalpy data.

C. Real-gas effects

The upward shift of high-enthalpy data evident in Figs. 19 and 21 arises from either an increase in measured L_{sep} due to effects not accounted for by the scaling, or an overprediction of the parameter group $M_1^3\gamma^{3/2}/\Lambda_1$ due to effects not accounted for by the external-flow computations. To convincingly attribute the discrepancy to real-gas effects, other possible causes must be eliminated. The difference cannot be accounted for by any reasonable systematic error in the methods used to predict the external flow parameters; one of the largest sources of error is uncertainty in the reservoir conditions, already included in the error bars shown in each figure. There is no reason effects due to three-dimensional flow should have significant dependence on stagnation enthalpy. The margin for error in flow-establishment estimations (see Sec. II D) was smaller for high-enthalpy conditions, but if separated flow were not established, the measured L_{sep} would be smaller, not larger.

Only condition C4 was expected to have significant driver-gas contamination (see Sec. II D 1), yet it is well correlated with the other high-enthalpy conditions in Fig. 19. This indicates two possibilities; either the degree of contamination in condition C4 was not significant, or contamination has only a weak effect on separation length. To estimate the magnitude of contamination effects on the parameter grouping used to scale separation length, a simple analysis was performed, consisting of a perfect-gas nozzle expansion followed by a perfect-gas wedge flow with various mass fractions of helium up to 50%. The procedure neglects any effect of the helium diluent on the nitrogen recombination rate which may change the free-stream composition. Taking Λ_1 to be approximately $(T_w/T_1)^{3/2}$, the largest relative change in the grouping $M_1^3\gamma_1^{3/2}(T_1/T_w)^{3/2}$ due to contamination was found to be on the order of a 15% reduction, consistent with the direction of the observed shift but far too small in magnitude. Flow history may also be important in determining the effects of contamination on separation length; if the separated flow is well established when helium arrives, then most of the helium flows past the separation zone without entering the recirculating region.

Despite the suggestive nature of a comparison between Figs. 19 and 20(b), the extensive arguments presented in Sec. VI A strongly discredit the possibility that the discrepancy could arise solely from the new scaling parameter Λ_1. Instead, Λ_1 serves to elucidate real-gas effects which are otherwise obscured.

External mechanisms for real-gas effects are already included in the L_{sep} scaling by use of external flow parameters from nonequilibrium external flow computations. The internal mechanism responsible for increased L_{sep} must arise from recombination occurring downstream of separation, because recombination effects on the upstream boundary layer were shown to be small in magnitude and cause a decrease in L_{sep} (see Sec. V B). The ratio of high-enthalpy to low-enthalpy data in Fig. 19 is approximately constant over a wide range of pressures ($p_2 \simeq 15-170\,\mathrm{kPa}$ among high-enthalpy experiments), despite significant differences in recombination rate (cases with $\theta_1 = 15°$ and high A_e/A_* have nearly frozen boundary layers) and degree of external dissociation ($0.11 < \alpha_1 < 0.25$ among high-enthalpy experiments). Thus it appears that the observed real-gas effect has little dependence on reaction rate or dissociation fraction. These parameters could not, however, be varied independently of one another in the experiments. In addition, no computations were performed in the present work to investigate the details of the mechanism causing increased L_{sep}. The present result is consistent with the computational results of Grumet *et al.*[48] for shock-impingement flows with $\alpha_1 > 0$. These showed a large increase in L_{sep} for high-pressure conditions with $p_1 = 123\,\mathrm{kPa}$ (which is of the same order as p_1 in the present experiments), and a slight decrease in L_{sep} for $p_1 = 143\,\mathrm{Pa}$ (with minimal recombination observed in the free-shear layer).

VII. CONCLUSIONS

Experiments were performed in the T5 Hypervelocity Shock Tunnel to investigate shock/boundary-layer interaction on a double wedge under high-enthalpy conditions with nitrogen test gas. Separation length was measured using flow visualization. Local inviscid external flow properties were estimated using a computational technique to account for thermochemical nonequilibrium and a nonuniform free stream. A new scaling parameter Λ_1 describing wall-temperature effects on separation length was developed for a nonreacting boundary layer by applying results from asymptotic theory to a simple force balance model, using the reference-temperature method to account for arbitrary viscosity law. A framework for describing real-gas effects on separation length was introduced which classifies mechanisms into those arising external or internal to viscous regions of the flow. The framework provides a context in which previous, present, and future results for real-gas effects on separated flow may be discussed.

External mechanisms were investigated by application of the ideal dissociating gas model to a scaling law for separation length based on local external flow properties. For dissociation occurring behind the reattachment shock but not behind the leading shock, the reattachment pressure decreases with respect to frozen flow and causes a decrease in separation length. For dissociation occurring behind the leading shock, the local Reynolds number, Mach number, and wall-to-edge temperature ratio at separation all increase with respect to frozen flow, but these have competing effects on the separation length. In addition, whether the reattachment pressure increases or decreases depends on the free-stream dissociation level. Thus the separation length may in general either increase or decrease, but appears to be affected under conditions of the present high-enthalpy experiments only at very high incidence, where a slight decrease is expected.

Internal mechanisms were further subdivided into those arising upstream or downstream of separation. The former were investigated by application of a thermochemical nonequilibrium Navier–Stokes code to flat-plate boundary layers under conditions of the present experiments, which encompassed only recombination-dominated boundary layers with partially dissociated edge conditions. Recombination near a cold wall was shown to increase skin friction (up to 5% under the present conditions) relative to a frozen boundary-layer with the same external dissociation level. According to the present theoretical model, this should cause a decrease in separation length. The mechanism has a small effect despite dissociation up to 25% in the local external flow at separation. Mechanisms arising downstream of separation were not analyzed in detail.

The experimental data for separation length were investigated by use of correlations based on local external parameters computed for reacting inviscid flow. This effectively scaled out external mechanisms. A linear dependence on the reattachment pressure ratio was found, in accordance with previous results for supersonic interactions in perfect-gas flow. A Reynolds-number effect due to transition moving upstream of reattachment was found for many of the low-enthalpy experiments. An increase in scaled separation length, approximately by a factor of 3, was observed for high-enthalpy laminar-interaction data with respect to low-enthalpy laminar-interaction data. The increase could only be recognized when the new parameter Λ_1 was included in the scaling to account for wall temperature effects on a nonreacting boundary layer. The increase was attributed to an internal mechanism arising downstream of separation. It was speculated that recombination in the free-shear layer or separation bubble under the present conditions decreases the shear stress along the dividing streamline.

It is important to emphasize that the observed real-gas effect appears to arise from the combination of free-stream dissociation and a cold wall, two conditions peculiar to shock tunnel experiments and not typically found in flight. It is also important to keep in mind the reference frozen flow; the observed internal mechanism induces an increase in separation length with respect to a frozen boundary layer with the same local external flow, even though that external flow may arise from nonequilibrium flow behind the leading shock. The complexity of the problem prohibits any general statement regarding separation length in practical flows which may combine internal and external mechanisms. Nevertheless, much progress has been achieved in understanding the physics of real-gas effects on separation.

ACKNOWLEDGMENTS

The authors wish to acknowledge Professor Hans Hornung, Professor Anatol Roshko, Professor Joseph Shepherd, and the late Professor Toshi Kubota for their insights, as well as the staff and students of the T5 Hypervelocity Shock Tunnel Laboratory for help setting up and running experiments. Special thanks are due Joseph Olejniczak for providing the computational code along with much invaluable advice on using and modifying it.

Cray supercomputer resources were provided through funding by NASA Offices of Mission to Planet Earth, Aeronautics, and Space Science. Experiments were funded by the Air Force Office of Scientific Research under Grant No. F49629-93-1-0338. Additional funding was provided by Caltech.

[1] J. B. Anders, ''Wedge-induced laminar-boundary-layer separation on a flat plate in low-density, hypervelocity flow,'' NASA Report No. TN-D-5791 (1970).
[2] A. W. Bloy and M. P. Georgeff, ''The hypersonic laminar boundary layer near sharp compression and expansion corners,'' J. Fluid Mech. **63**, 431 (1974).
[3] G. T. Coleman and J. L. Stollery, ''Heat transfer from hypersonic turbulent flow at a wedge compression corner,'' J. Fluid Mech. **56**, 741 (1972).
[4] G. M. Elfstrom, ''Turbulent hypersonic flow at a wedge-compression corner,'' J. Fluid Mech. **53**, 113 (1972).
[5] H. Ferguson and J. W. Schaefer, ''Heat transfer and pressure distribution on cone-cylinder-flare configuration with boundary-layer separation,'' NASA Report No. TN-D-1436 (1962).
[6] G. E. Gadd, D. W. Holder, and J. D. Regan, ''An experimental investigation of the interaction between shock waves and boundary layers,'' Proc. R. Soc. London, Ser. A **226**, 227 (1954).
[7] W. D. Harvey, ''Experimental investigation of laminar-flow separation on a flat plate induced by deflected trailing-edge flap at Mach 19,'' NASA Report No. TN-D-4671 (1968).
[8] K. Hayakawa and L. C. Squire, ''The effect of the upstream boundary-layer state on the shock interaction at a compression corner,'' J. Fluid Mech. **122**, 369 (1982).
[9] M. Holden, ''A study of flow separation in regions of shock wave-boundary layer interaction in hypersonic flow,'' AIAA Pap. No. 78-1169 (1978).
[10] D. Kumar and J. L. Stollery, ''Hypersonic control flap effectiveness,'' ICAS Paper No. 94-4.4.3, presented at the Nineteenth International Council of the Aeronautical Sciences Congress in Anaheim, CA, 18–23 September 1994.
[11] D. S. Miller, R. Hijman, and M. E. Childs, ''Mach 8 to 22 studies of flow separations due to deflected control surfaces,'' AIAA J. **2**, 312 (1964).
[12] D. A. Needham, ''Laminar separation in hypersonic flow,'' Ph.D. thesis, University of London, 1965.
[13] A. Roshko and G. J. Thomke, ''Supersonic, turbulent boundary-layer interaction with a compression corner at very high Reynolds number,'' in *Viscous Interaction Phenomena in Supersonic and Hypersonic Flow* (University of Dayton Press, Dayton, 1970).
[14] G. S. Settles, T. J. Fitzpatrick, and S. M. Bogdonoff, ''Detailed study of attached and separated compression corner flowfields in high Reynolds number supersonic flow,'' AIAA J. **17**, 579 (1979).
[15] G. S. Settles and S. M. Bogdonoff, ''Scaling of two- and three-dimensional shock/turbulent boundary-layer interactions at compression corners,'' AIAA J. **20**, 782 (1982).
[16] J. F. Fay and J. Sambamurthi, ''Laminar hypersonic flow over a compression corner using the HANA code,'' AIAA Pap. No. 92-2896 (1992).
[17] F. Grasso and G. Leone, ''Chemistry effects in shock wave boundary layer interaction problems,'' in *Proceedings of the IUTAM Symposium on Aerothermochemistry of Spacecraft and Associated Hypersonic Flows* (Jouve, Paris, 1992).
[18] E. Katzer, ''On the length scales of laminar shock/boundary-layer interaction,'' J. Fluid Mech. **206**, 477 (1989).
[19] J. N. Nielsen, F. K. Goodwin, and G. D. Kuhn, ''Review of the method of integral relations applied to viscous interaction problems including separation,'' in Ref. 13.
[20] D. P. Rizzetta, O. R. Burggraf, and R. Jenson, ''Triple-deck solutions for viscous supersonic and hypersonic flow past corners,'' J. Fluid Mech. **89**, 535 (1978).
[21] J. B. Anders and C. L. W. Edwards, ''A real-gas study of low-density wedge-induced laminar separation on a highly cooled blunt flat plate at $M_\infty = 12$,'' NASA Report No. TN-D-4320 (1968).
[22] M. S. Holden, ''Boundary-layer displacement and leading-edge bluntness effects on attached and separated laminar boundary layers in a compression corner. II. Experimental study,'' AIAA J. **9**, 84 (1971).
[23] M. S. Holden, ''Shock wave-turbulent boundary layer interaction in hypersonic flow,'' AIAA Pap. No. 72-74 (1972).
[24] A. Roshko and G. J. Thomke, ''Flare-induced interaction lengths in supersonic, turbulent boundary layers,'' AIAA J. **14**, 873 (1976).
[25] C. B. Johnson, ''Pressure and flow-field study at Mach number 8 of flow separation on a flat plate with deflected trailing-edge flap,'' NASA 4308 (1968).
[26] J. E. Lewis, T. Kubota, and L. Lees, ''Experimental investigation of supersonic laminar, two-dimensional boundary-layer separation in a compression corner with and without cooling,'' AIAA J. **6**, 7 (1968).
[27] D. A. Needham and J. L. Stollery, ''Boundary layer separation in hypersonic flow,'' AIAA Pap. No. 66-455 (1966).
[28] A. Todisco and B. L. Reeves, ''Turbulent boundary layer separation and reattachment at supersonic and hypersonic speeds,'' in Ref. 13.
[29] L. G. Hunter, Jr. and B. L. Reeves, ''Results of a strong interaction, wake-like model of supersonic separated and reattaching turbulent flows,'' AIAA J. **9**, 703 (1971).
[30] S. N. Brown, H. K. Cheng, and C. J. Lee, ''Inviscid-viscous interaction on triple-deck scales in a hypersonic flow with strong wall cooling,'' J. Fluid Mech. **220**, 309 (1990).
[31] M. Coët and B. Chanetz, ''Experiments on shock wave/boundary layer interaction in hypersonic flow,'' Rech. Aerosp. (English edition) **1**, 61 (1993).
[32] N. Curle, ''The effects of heat transfer on laminar-boundary-layer separation in supersonic flow,'' Aeronaut. Q. **12**, 309 (1961).
[33] M. P. Georgeff, ''Momentum integral method for viscous-inviscid interactions with arbitrary wall cooling,'' AIAA J. **12**, 1393 (1974).
[34] J. P. Rayner, ''Boundary layer separation and thermal choking,'' Ph.D. thesis, Australian National University, 1973.
[35] K. C. A. Crane and R. J. Stalker, ''Mass-spectrometric analysis of hypersonic flows,'' J. Phys. D **10**, 679 (1977).
[36] S. G. Mallinson, S. L. Gai, and N. R. Mudford, ''Upstream influence and peak heating in hypervelocity shock wave/boundary-layer interaction,'' J. Propul. Power **12**, 984 (1996).
[37] S. G. Mallinson, S. L. Gai, and N. R. Mudford, ''The interaction of a shock wave with a laminar boundary layer at a compression corner in high-enthalpy flows including real gas effects,'' J. Fluid Mech. **342**, 1 (1997).
[38] S. R. Sanderson, ''Shock wave interaction in hypervelocity flow,'' Ph.D. thesis, California Institute of Technology, 1995.
[39] S. G. Mallinson, S. L. Gai, and N. R. Mudford, ''The boundary layer on a flat plate in hypervelocity flow,'' Aeronaut. J. **100**, 135 (1996).
[40] R. Krek, W. Beck, and G. Eitelberg, ''Hyperboloid flare experiments in the HEG,'' in *Proceedings of the 20th International Symposium on Shock Waves* (World Scientific, Singapore, 1996).
[41] J. Davis, ''Further tests on the HALIS axisymmetric configuration in the T5 hypervelocity shock tunnel,'' GALCIT Technical Report No. FM 96-2, Graduate Aeronautical Laboratories, California Institute of Technology (1996).

[42] G. Brenner, T. Gerhold, K. Hannemann, and D. Rues, ''Numerical simulation of shock/shock and shock-wave/boundary-layer interactions in hypersonic flows,'' Comput. Fluids **22**, 427 (1993).
[43] J. Oswald, A. Demargne, and J. Bousqet, ''Hypersonic laminar computations of separated flows with account of real gas effects,'' AIAA Pap. No. 95-2271 (1995).
[44] W. Kordulla, S. Riedelbauch, G. Brenner, and U. Prinz, ''Hypersonic viscous flow simulations,'' Fluid Dyn. Res. **10**, 451 (1992).
[45] G. H. Furumoto, X. Zhong, and J. C. Skiba, ''Numerical studies of real-gas effects on two-dimensional hypersonic shock-wave/boundary-layer interaction,'' Phys. Fluids **9**, 191 (1997).
[46] H. Ikawa, ''Real gas laminar boundary layer separation methodology as applied to orbiter control surface effectiveness prediction,'' AIAA Pap. No. 79-0212 (1979).
[47] C. A. Ballaro and J. D. Anderson, Jr., ''Shock strength effects on separated flows in non-equilibrium chemically reacting air shock wave/boundary layer interaction,'' AIAA Pap. No. 91-0250 (1991).
[48] A. Grumet, J. D. Anderson, Jr., and M. J. Lewis, ''Numerical study of the effects of wall catalysis on shock wave/boundary-layer interaction,'' J. Thermophys. Heat Transfer **8**, 40 (1994).
[49] H. Hornung and J. Bélanger, ''Role and techniques of ground testing for simulation of flows up to orbital speed,'' AIAA Pap. No. 90-1377 (1990).
[50] H. Hornung, B. Sturtevant, J. Bélanger, S. Sanderson, and M. Brouillette, ''Performance data of the new free-piston shock tunnel T5 at GALCIT,'' in *Proceedings of the 18th International Symposium on Shock Waves* (Springer, Berlin, 1991).
[51] H. Hornung, ''Performance data of the new free-piston shock tunnel at GALCIT,'' AIAA Pap. No. 92-3943 (1992).
[52] M. K. McIntosh, ''A computer program for the numerical calculation of equilibrium and perfect gas conditions in shock tunnels,'' Australian Defense Scientific Service Tech. Note No. CPD 169, 1979.
[53] D. A. Needham and J. L. Stollery, ''Hypersonic studies of incipient separation and separated flows,'' in *Separated Flows, Part I* (AGARD CP-4, 1966).
[54] K. O. W. Ball and R. H. Korkegi, ''An investigation of the effect of suction on hypersonic laminar boundary-layer separation,'' AIAA J. **6**, 239 (1968).
[55] J. Davis, ''High-enthalpy shock/boundary-layer interaction on a double wedge,'' Ph.D. thesis, California Institute of Technology, 1999.
[56] B. Sundqvist, ''Thermal diffusivity and thermal conductivity of chromel, alumel, and constantan in the range 100–450 K,'' J. Appl. Phys. **72**, 539 (1992).
[57] S. G. Mallinson, S. L. Gai, and N. R. Mudford, ''Establishment of steady separated flow over a compression-corner in a free-piston shock tunnel,'' Shock Waves **7**, 249 (1997).
[58] L. Davies and J. L. Wilson, ''Influence of reflected shock and boundary-layer interaction on shock-tube flows,'' Phys. Fluids **12**, 37 (1969).
[59] N. Sudani and H. G. Hornung, ''Gas dynamical detectors of driver gas contamination in a high-enthalpy shock tunnel,'' AIAA J. **36**, 313 (1998).
[60] N. Sudani and H. G. Hornung, ''Detection and reduction of driver gas contamination in a high-enthalpy shock tunnel,'' in *Proceedings of the 21st International Symposium on Shock Waves* (Panther, Fyshwick, Australia, 1997).
[61] N. Sudani, B. Valiferdowsi, and H. G. Hornung, ''Test time increase by delaying driver gas contamination for reflected shock tunnels,'' AIAA Pap. No. 98-2771 (1998).
[62] B. Chanetz and M.-C. Coët, ''Shock wave boundary layer interaction analyzed in the R5Ch laminar hypersonic wind tunnel,'' Rech. Aerosp. (English edition) **5**, 43 (1993).
[63] V. I. Kornilov, ''Correlation of the separation length in shock wave/channel boundary layer interaction,'' Exp. Fluids **23**, 489 (1997).
[64] W. L. Hankey and M. S. Holden, ''Two-dimensional shock wave-boundary layer interactions in high speed flows,'' AGARD AG-203 (1975).
[65] K. O. W. Ball, ''Flap span effects on boundary-layer separation,'' AIAA J. **9**, 2080 (1971).
[66] J. J. Ginoux, ''Streamwise vortices in laminar flow,'' in *Recent Developments in Boundary Layer Research, Part I* (AGARDograph No. 97, 1965).
[67] A. Henckels, A. F. Kreins, and F. Maurer, ''Experimental investigations of hypersonic shock-boundary layer interaction,'' Z. Flugwiss. Weltraumforsch. **17**, 116 (1993).
[68] J. Olejniczak, ''Computational and experimental study of nonequilibrium chemistry in hypersonic flows,'' Ph.D. thesis, University of Minnesota, 1997.
[69] G. Candler, ''The computation of weakly ionized hypersonic flows in thermo-chemical nonequilibrium,'' Ph.D. thesis, Stanford University, 1988.
[70] E. P. Bartlett, R. M. Kendall, and R. A. Rindal, ''An analysis of the coupled chemically reacting boundary layer and charing ablator. IV. A unified approximation for mixture transport properties for multicomponent boundary layer applications,'' NASA Report No. CR-1063 (1968).
[71] R. G. Gupta, J. M. Yos, R. A. Thompson, and K. Lee, ''A review of reaction rates and thermodynamic and transport properties for an 11-species air model for chemical and thermal nonequilibrium calculations to 30000 K,'' NASA Report No. RP-1232 (1990).
[72] R. C. Millikan and D. R. White, ''Systematics of vibrational relaxation,'' J. Chem. Phys. **39**, 3209 (1963).
[73] C. Park, ''Assessment of a two-temperature model for dissociating and weakly ionizing nitrogen,'' J. Thermophys. Heat Transfer **2**, 8 (1988).
[74] C. Park, ''Two-temperature interpretation of dissociation rate data for N_2 and O_2,'' AIAA Pap. No. 88-0458 (1988).
[75] R. W. MacCormack and G. V. Candler, ''The solution of the Navier–Stokes equations using Gauss–Seidel line relaxation,'' Comput. Fluids **17**, 135 (1989).
[76] K. Hannemann, R. Krek, and G. Eitelberg, ''Latest calibration results of the HEG contoured nozzle,'' in Ref. 40.
[77] S. Brück and K. Hannemann, ''The effect of nozzle-flow disturbances on shock wave/boundary layer interaction,'' in Ref. 60.
[78] W. H. Dorrance, *Viscous Hypersonic Flow* (McGraw-Hill, New York, 1962).
[79] F. G. Blottner, M. Johnson, and M. Ellis, ''Chemically reacting viscous flow program for multi-component gas mixtures,'' Sandia National Laboratories Report No. SC-RR-70-754, 1971.
[80] C. R. Wilke, ''A viscosity equation for gas mixtures,'' J. Chem. Phys. **18**, 517 (1950).
[81] C. M. Hung and R. W. MacCormack, ''Numerical solutions of supersonic and hypersonic laminar compression corner flows,'' AIAA J. **14**, 475 (1976).
[82] P. Leyland, ''Shock-wave/boundary layer interactions at hypersonic speed by an implicit Navier–Stokes solver,'' Computational Fluid Dyn. **6**, 71 (1996).
[83] G. D. Power and T. J. Barber, ''Analysis of complex hypersonic flows with strong viscous/inviscid interaction,'' AIAA J. **26**, 832 (1988).
[84] R. Ramakrishnan, E. A. Thornton, and A. R. Wieting, ''Adaptive finite element analysis of hypersonic laminar flows for aerothermal load predictions,'' J. Thermophys. **5**, 308 (1991).
[85] F. Grasso and M. Marini, ''Analysis of hypersonic shock-wave laminar boundary-layer interaction phenomena,'' Comput. Fluids **25**, 561 (1996).
[86] F. Grasso, G. Leone, and J. M. Délery, ''Validation procedure for the analysis of shock-wave/boundary-layer interaction problems,'' AIAA J. **32**, 1820 (1994).
[87] D. Rizzetta and K. Mach, ''Comparative numerical study of hypersonic compression ramp flows,'' AIAA Pap. No. 89-1877 (1989).
[88] G. Simeonides, W. Haase, and M. Mann, ''Experimental, analytical, and computational methods applied to hypersonic compression ramp flows,'' AIAA J. **32**, 301 (1994).
[89] J. L. Thomas, ''An implicit multigrid scheme for hypersonic strong-interaction flow fields,'' Commun. Appl. Num. Methods **8**, 683 (1992).
[90] M. S. Holden and J. R. Moselle, ''Theoretical and experimental studies of the shock wave-boundary layer interaction on compression surfaces in hypersonic flow,'' Aerospace Research Laboratories, USAF-OAR Report No. ARL-70-0002, 1968.
[91] D. H. Rudy, J. L. Thomas, A. Kumar, and P. A. Gnoffo, ''Computation of laminar hypersonic compression-corner flows,'' AIAA J. **29**, 1108 (1989).
[92] J. Y. Lee and M. J. Lewis, ''Numerical study of the flow establishment time in hypersonic shock tunnels,'' J. Spacecr. Rockets **30**, 152 (1993).
[93] F. M. White and G. H. Christoph, ''A simple theory for the two-dimensional compressible turbulent boundary layer,'' J. Basic Eng. **94**, 636 (1972).
[94] H. S. Glick, ''Modified Crocco–Lees mixing theory for supersonic separated and reattaching flows,'' J. Aerosp. Sci. **29**, 1238 (1962).
[95] D. R. Chapman, D. M. Kuehn, and H. K. Larson, ''Investigation of separated flows in supersonic and subsonic streams with emphasis on the effect of transition,'' NACA Report No. R-1356 (1958).

[96] D. R. Chapman and H. H. Korst, ''Theory for base pressures in transonic and supersonic flow,'' J. Appl. Mech. **24**, 484 (1957).
[97] J. F. Nash, ''An analysis of two-dimensional base flow including the effect of the approaching boundary layer,'' Aeronautical Research Council R&M No. 3344, 1963.
[98] H. McDonald, ''Turbulent shear layer re-attachment with special emphasis on the base pressure problem,'' Aeronaut. Q. **15**, 247 (1964).
[99] V. V. Sychev, ''Asymptotic theory of separation flows,'' Fluid Dyn. (English translation of Izv. Akad. Nauk SSSR, Mekh. Zhid. Gaza), **17**, 179 (1982).
[100] A. Roshko, ''Free shear layers, base pressure and bluff-body drag,'' in *Symposium on Developments in Fluid Dynamics and Aerospace Engineering* (Interline, Bangalore, 1995).
[101] R. J. Hakkinen, I. Greber, L. Trilling, and S. S. Abarbanel, ''The interaction of an oblique shock wave with a laminar boundary layer,'' NASA Tech. Memo No. 2-18-59W (1959).
[102] D. Kumar, ''Hypersonic control effectiveness,'' Ph.D. thesis, Cranfield University, 1995.
[103] O. R. Burggraf, ''Asymptotic theory of separation and reattachment of a laminar boundary layer on a compression ramp,'' in *Flow Separation* (AGARD CP-168, 1975).
[104] G. R. Inger, ''Scaling of incipient separation in supersonic/transonic speed laminar flows,'' AIAA J. **33**, 227 (1994).
[105] G. R. Inger, ''Scaling of incipient separation in high speed laminar flows,'' Aeronaut. J. **98**, 178 (1994).
[106] K. Stewartson and P. G. Williams, ''Self-induced separation,'' Proc. R. Soc. London, Ser. A **312**, 181 (1969).
[107] K. Stewartson and P. G. Williams, ''On self-induced separation. II,'' Mathematika **20**, 98 (1973).
[108] V. Y. Neiland, ''Flow behind the boundary layer separation point in a supersonic stream,'' Fluid Dyn. [English translation of Izv. Akad. Nauk SSSR, Mekh. Zhid. Gaza **3**, 19 (1971)].
[109] M. J. Lighthill, ''Dynamics of a dissociating gas. I,'' J. Fluid Mech. **2**, 1 (1957).
[110] H. G. Hornung, ''Ae234 class notes (Hypersonic Aerodynamics),'' California Institute of Technology, 1996.
[111] W. G. Vincenti and C. H. Kruger, *Introduction to Physical Gas Dynamics* (Krieger, New York, 1965).
[112] W. J. Rae, ''A solution for the nonequilibrium flat-plate boundary layer,'' AIAA J. **1**, 2279 (1963).
[113] D. F. Rogers, *Laminar Flow Analysis* (Cambridge University Press, Cambridge, 1992).
[114] F. G. Blottner, ''Chemical nonequilibrium boundary layer,'' AIAA J. **2**, 232 (1964).
[115] G. R. Inger, ''Nonequilibrium boundary-layer effects on the aerodynamic heating of hypersonic waverider vehicles,'' J. Thermophys. Heat Transfer **9**, 595 (1995).
[116] G. R. Inger, ''Non-equilibrium boundary layer effects on the aerodynamic heating of hypersonic vehicles,'' Acta Astron. **36**, 205 (1995).
[117] G. R. Inger, ''Highly nonequilibrium boundary-layer flows of a multicomponent dissociated gas mixture,'' Int. J. Heat Mass Transf. **7**, 1151 (1964).
[118] L. L. Moore, ''A solution of the laminar boundary-layer equations for a compressible fluid with variable properties, including dissociation,'' J. Aeronaut. Sci. **19**, 505 (1952).
[119] L. J. Crane, ''The laminar and turbulent mixing of jets of compressible fluid. II. The mixing of two semi-infinite streams,'' J. Fluid Mech. **3**, 81 (1957).
[120] R. D. Mills, ''Numerical and experimental investigations of the shear layer between two parallel streams,'' J. Fluid Mech. **33**, 591 (1968).
[121] M. R. Denison and E. Baum, ''Compressible free shear layer with finite initial thickness,'' AIAA J. **1**, 342 (1963).
[122] C. A. Kennedy and T. B. Gatski, ''Self-similar supersonic variable-density shear layers in binary systems,'' Phys. Fluids **6**, 662 (1994).
[123] G. E. Dieter, *Engineering Design: A Materials and Processing Approach*, 2nd ed. (McGraw–Hill, New York, 1991).
[124] H. K. Larson and S. J. Keating, Jr, ''Transition Reynolds numbers of separated flows at supersonic speeds,'' NASA Report No. TN-D-349 (1960).
[125] R. A. King, J. Creel, and D. M. Bushnell, ''Experimental transition investigation of a free-shear layer above a cavity at Mach 3.5,'' J. Propul. Power **7**, 626 (1991).
[126] S. F. Birch and J. W. Keyes, ''Transition in compressible free shear layers,'' J. Spacecr. Rockets **9**, 623 (1972).